

**The new GFDL global atmosphere and land model AM2/LM2:
Evaluation with prescribed SST simulations**

GFDL's Global Atmospheric Model Development Team (GAMDT)

Jeffrey L. Anderson⁺, V. Balaji[&], Anthony J. Broccoli[^], William F. Cooke[%],
Thomas L. Delworth⁺, Keith W. Dixon⁺, Leo J. Donner⁺, Krista A. Dunne[#],
Stuart M. Freidenreich⁺, Stephen T. Garner⁺, Richard G. Gudgel⁺, C. T. Gordon⁺,
Isaac M. Held⁺, Richard S. Hemler⁺, Larry W. Horowitz⁺, Stephen A. Klein^{+*},
Thomas R. Knutson⁺, Paul J. Kushner^{+*}, Amy R. Langenhorst[%], Ngar-Cheung Lau⁺, Zhi Liang[%],
Sergey L. Malyshev[@], P. C. D. Milly[#], Mary J. Nath⁺, Jeffrey J. Ploshay⁺, V. Ramaswamy⁺,
M. Daniel Schwarzkopf⁺, Elena Shevliakova[@], Joseph J. Sirutis⁺, Brian J. Soden⁺, William F. Stern⁺,
Lori A. Thompson[%], R. John Wilson⁺, Andrew T. Wittenberg^{\$}, and Bruce L. Wyman⁺

⁺*Geophysical Fluid Dynamics Laboratory
National Oceanic and Atmospheric Administration
Princeton, New Jersey*

[&]*Silicon Graphics Incorporated
Princeton, New Jersey*

[%]*RSIS
McLean, Virginia,
presently at GFDL*

[#]*U.S. Geological Survey
Princeton, New Jersey*

^{\$}*Atmospheric and Oceanic Sciences Visiting Scientists Program
Princeton University
Princeton, New Jersey*

[@]*Department of Ecology and Evolutionary Biology
Princeton University
Princeton, New Jersey*

Submitted to *Journal of Climate*, March 2003

*Corresponding authors and team leaders: Stephen A. Klein and Paul J. Kushner, Geophysical Fluid Dynamics Laboratory/NOAA, Princeton University Forrestal Campus/ US Route 1, P.O.Box 308, Princeton, New Jersey 08542, e-mail: Stephen.Klein@gfdl.noaa.gov and Paul.Kushner@gfdl.noaa.gov

[^]Now at Department of Environmental Sciences, Rutgers University, New Brunswick, New Jersey.

Abstract

The configuration and performance of a new global atmosphere and land model developed at the Geophysical Fluid Dynamics Laboratory (GFDL) for climate research is presented. The atmosphere model, known as AM2, includes a new gridpoint dynamical core, a prognostic cloud scheme, and a multi-species aerosol climatology, as well as components from previous models used at GFDL. The land model, known as LM2, includes soil heat storage, groundwater storage, and stomatal effects. The performance of the coupled model AM2/LM2 is evaluated with a series of prescribed sea-surface temperature (SST) simulations. Particular focus is given to the model's climatology and the characteristics of interannual variability related to El Niño/Southern Oscillation (ENSO).

One of the integrations was performed according to the prescriptions of the second Atmospheric Model Intercomparison Project (AMIP II) and data were submitted to the Program for Climate Model Diagnosis and Intercomparison (PCMDI). Particular strengths of AM2/LM2, as judged by comparison to other models participating in AMIP II, include a commendable simulation of the shortwave radiation budget and temperatures in the extratropical lower stratosphere near 200 hPa. Distinct weaknesses of AM2/LM2, as compared to other AMIP II models, include midlatitude oceanic westerly wind stresses that are shifted equatorward and a tendency towards a double Intertropical Convergence Zone (ITCZ) in the Pacific. Other prominent problems include unrealistically weak tropical transient activity, a positive Arctic sea level pressure (SLP) bias, and excessive wintertime cloudiness over high latitude continents.

An ensemble of 10 integrations with observed SSTs for the second half of the twentieth

century permits a statistically reliable assessment of the model's response to ENSO. Although the model produces credible precipitation anomalies in the tropical Pacific and Asian sectors, the response of the geopotential height in the North Pacific and North American sector is unrealistically weak.

1. Introduction

In this report, an overview is presented of the new GFDL global atmosphere and land model known as "AM2/LM2". AM2 and LM2 are, respectively, the atmospheric and terrestrial components of the earth-system model that is under development at GFDL for climate research and climate prediction applications. In developing AM2/LM2, the focus has been on consolidating and improving the various versions of such models that have been used in GFDL's past (Hamilton et al. 1995, Stern and Miyakoda 1995, Delworth et al. 2002). The principal aim is to create a model that represents realistically the dynamic, thermodynamic, and radiative characteristics of the climate system and is suitable for coupling to ocean and sea-ice models without flux adjustment. Balanced against this aim is the need to have a model computationally fast enough so that ensemble multi-century integrations may be performed.

Although AM2/LM2 incorporates many important pieces of previous models used within GFDL, it does represent a substantial break from the past. AM2 includes a new gridpoint atmospheric dynamical core, a multi-species three dimensional aerosol climatology, and a fully prognostic cloud scheme. LM2 incorporates soil heat storage, groundwater storage, stomatal control of transpiration, and soil and plant dependent parameters. These new components have required modification and retuning of those pieces of the components that were carried over from previous models. This has led to a model with more capabilities and potential for growth as well as a model with simulation characteristics generally superior to that of the older GFDL models.

Our model development effort is team-based and involves a broad cross section of expertise from within and outside of GFDL; this has required a challenging degree of coordination. A

simultaneous challenge has been GFDL's transition from vector to parallel computing architectures. To address these challenges, an in-house software framework known as the "Flexible Modeling System" (FMS, <http://www.gfdl.noaa.gov/~fms>) has been developed. FMS based codes are modular, use Fortran 90, and are based on standardized interfaces between component models (i.e. land, atmosphere, ocean, sea-ice). The software conservatively passes the fluxes of heat, moisture, and momentum between component models which may have different horizontal grids. The FMS code organization isolates those aspects of the code related to parallel computing to a relatively simple message passing interface (<http://www.gfdl.noaa.gov/~vb/mpp.html>). As a result, scientists developing new code for the model need not learn the intricacies of parallel computing. Using the FMS, it has been possible to rapidly test a variety of model configurations and follow parallel development paths for the atmosphere, ocean, land, and sea-ice models. FMS models have been tested simultaneously on vector and parallel platforms. As a consequence, the transition to a new parallel computing environment was made with relative ease.

Section 2 of the report documents the components of AM2/LM2 as well as the boundary conditions for the experiments performed. Section 3 provides a discussion of AM2/LM2's climatological circulation, hydrology and radiation budget, as well as its variability. A brief comparison of the quality of AM2/LM2's climatology to that of other models is given in section 4 while future plans are discussed in section 5.

2. Model components and boundary conditions

The components of AM2/LM2 are described in the following three subsections. For ease of reference, a summary of model components is given in Table 1.

GFDL GAMDT

a. Grid-point dynamical core

The hydrostatic, finite difference dynamical core has been developed from models described in Mesinger et al. (1988) and Wyman (1996). The AM2/LM2 dynamical core solves the equations for the same set of prognostic variables as in these references, but uses a different horizontal and vertical grid. The latitude-longitude horizontal grid is the staggered Arakawa B-grid (Arakawa and Lamb 1977) with resolution 2.5° longitude by 2° latitude. In the vertical, a hybrid coordinate grid is used; sigma surfaces near the ground continuously transform to pressure surfaces above 250 hPa (Table 2). The model has 18 vertical levels with the lowest model level about 30 meters above the surface. Five levels are in the stratosphere with the top level at about 3 hPa. The prognostic variables are the zonal and meridional wind components, surface pressure, temperature, and tracers. The tracers include specific humidity and three prognostic cloud variables (section 2b3).

The model utilizes a two-level time differencing scheme. Gravity waves are integrated using the forward-backward scheme (Mesinger 1977) and a split time differencing scheme is used for longer advective and physics time steps (Gadd 1978). The advective terms are integrated with a modified Euler backward scheme that has less damping than the full backward scheme (Kurihara and Tripoli 1976). Note that the Euler backward scheme is needed for stability. The gravity wave, advective and physics time steps are 200, 600, and 1800 seconds, respectively.

The energy and angular momentum conserving vertical finite difference scheme used is from Simmons and Burridge (1981). Horizontal advection uses centered spatial differencing. Momentum advection is fourth-order; temperature and tracer advection is second-order. The vertical advection of tracers use a piecewise linear finite volume scheme (Lin et al. 1994). Grid point

noise and the $2\Delta x$ computational mode of the B-grid are controlled with linear fourth-order horizontal diffusion. A term is added to the diffusive fluxes of heat and moisture to prevent spurious diffusion up sloping model surfaces. A second order Shapiro (1970) filter is applied to the departures from the zonal mean of the zonal wind component and to the total meridional wind component at the top model level to reduce the reflection of waves. Fourier filtering is applied poleward of 60° latitude to damp the shortest resolvable waves so that a longer time step can be taken. The filter is applied to the mass divergence, the horizontal omega-alpha term, the horizontal advective tendencies, and the momentum components.

Excluding the dissipation terms and time differencing, the numerical schemes are designed to conserve total energy. To guarantee energy conservation for long climate runs, a global energy correction is applied to temperature.

b. Atmospheric physics

1) RADIATION AND PRESCRIBED OZONE AND AEROSOL CLIMATOLOGIES

The shortwave radiation algorithm follows Freidenreich and Ramaswamy (1999; hereinafter FR99), with the following modifications. With a view towards computational efficiency, the band structure and the number of exponential-sum fit terms within some bands have been altered, resulting in fewer pseudo-monochromatic columnar calculations. Specifically, the band from 0-2500 cm^{-1} now has one instead of six terms, owing to consideration of CO_2 as the only absorber for this interval; there is one band from 2500-4200 cm^{-1} instead of three, and the total number of terms is reduced from twelve to eight; there is one band from 4200 to 8200 cm^{-1} instead of four, and the total number of terms is reduced from twenty-four to nine; the number of terms for the

GFDL GAMDT

8200-11500 cm^{-1} band is reduced from seven to five while that for the 11500-14600 cm^{-1} band is reduced from eight to two; there are three bands between 27500 and 34500 cm^{-1} (viz., 27500 to 32400, 32400 to 33300 and 33300 to 34500) instead of five, each with one term. The number of bands in the solar spectrum is reduced from twenty-five to eighteen, while the total pseudo-monochromatic column calculations required per grid-box is reduced from seventy-two to thirty-eight. The new band structure and the revised exponential-sum fits have been developed and tested using the 'benchmark' calculations described in FR99. The maximum error in the clear-sky heating rates is about 15%, a moderate increase from the less than 10% error obtained with the seventy-two-term fit. The errors in the shortwave overcast sky heating rates for the water cloud model considered (Slingo 1989) are now ~15%, increased from ~10% for the 72-term fit; for ice clouds, the errors tend to be larger (FR99) and for the present parameterization could reach ~25%.

The interactions considered include absorption by H_2O , CO_2 , O_3 , O_2 , molecular scattering, and absorption and scattering by aerosols and clouds. For water clouds, the single-scattering properties in the solar spectrum follow Slingo (1989); for ice clouds, the formulation follows Fu and Liou (1993). Three-dimensional, monthly-mean profiles of aerosol mass concentrations and their optical properties follow Haywood et al. (1999) and Haywood (personal communication). The prescription accounts for sea-salt (low windspeed case) and the natural and anthropogenic components of dust, carbonaceous (black and organic carbon) aerosol, and sulfate.

Ozone profiles follow Fortuin and Kelder (1998) and are based on observations over the 1989-1991 period. This climatology has been shown to yield results that represent substantial improvements over those obtained with previous older climatologies used in the GFDL global models (Ramaswamy and Schwarzkopf 2002).

GFDL GAMDT

The ocean surface is assumed to be Lambertian, with the albedo being a function of the solar zenith angle following the formulation of Taylor et al. (1996).

The band-averaging of the single-scattering parameters is performed using the thick-averaging technique (Edwards and Slingo 1996). The delta-Eddington technique is employed to compute the layer reflection and transmission based on the single-scattering properties of that layer (FR99). The diffuse incident beam is assumed to be isotropic and its reflection and transmission is computed using an effective angle of 53° , in contrast to the 4-point quadrature scheme in FR99. The net direct and diffuse quantities in each layer is given by the weighted sum of the clear and overcast sky fractions present in that layer. The fluxes and heating rates are computed using an "adding" scheme (Ramaswamy and Bowen 1994).

The longwave radiation code follows the modified form of the Simplified Exchange Approximation and is also developed and tested using 'benchmark' computations (Schwarzkopf and Ramaswamy 1999). It accounts for the absorption and emission by the principal gases in the atmosphere, including H_2O , CO_2 , O_3 , N_2O , CH_4 , and the halocarbons CFC-11, CFC-12, CFC-113 and HCFC-22. For the water vapor continuum, the CKD 2.1 formulation of Clough et al. (1992) is used. Aerosols and clouds are treated as absorbers in the longwave, with non-grey absorption coefficients specified in the eight spectral bands of the transfer scheme, following the methodology adopted in Ramachandran et al. (2000). For water clouds, the absorption coefficients follow those employed in Held et al. (1993) while, for ice, the Fu and Liou (1993) prescription is used.

2) CUMULUS PARAMETERIZATION

Moist convection is represented by the Relaxed Arakawa-Schubert (RAS) formulation of

GFDL GAMDT

Moorthi and Suarez (1992), with the following modifications. (a) The fraction of water condensed in the cumulus updrafts which becomes precipitation (known as the 'precipitation efficiency') is specified to be 0.986 for deep convection and 0.1 for shallow convection. Deep convection is defined as updrafts which detrain at pressure levels above 500 hPa whereas shallow convection is defined as updrafts which detrain beneath 800 hPa. For pressures between 500 and 800 hPa, the precipitation efficiency is linearly interpolated in pressure between the values for deep and shallow convection. Note that this version of RAS lacks cumulus updraft microphysics such as that developed by Sud and Walker (1999). (b) The non-precipitated fraction of condensed water, 0.014 for deep convection and 0.9 for shallow convection, is a source of condensate for the prognostic cloud scheme. (c) Re-evaporation of convective precipitation is allowed to occur. Note that this version of RAS does not include the effects of convective downdrafts developed by Moorthi and Suarez (1999) in a later version. (d) The time scale over which the cloud work function is relaxed to a cloud type dependent value is modified so that deep updrafts relax over a time scale of about 12 hours but shallow updrafts relax over a time scale of only 2 hours. (e) The cloud type dependent cloud work function is based upon observations (Lord and Arakawa 1980) but enhanced by 40% to encourage increased tropical transient activity.

3) CLOUD SCHEME

Large-scale clouds are parameterized with separate prognostic variables for the liquid and ice specific humidities. Cloud fraction is also treated as a prognostic variable of the model following the parameterization of Tiedtke (1993). Cloud microphysics are parameterized according to Rotstayn (1997) with an updated treatment of mixed phase clouds (Rotstayn et al. 2000). Fluxes of large-scale rain and snow are diagnosed and the amount of precipitation flux inside and outside

of clouds is tracked separately (Jakob and Klein 2000). The particle size needed for radiation calculations of liquid clouds is diagnosed from the prognosed liquid water content and an assumed cloud droplet number concentration which is specified from observations to be 250 cm^{-3} over land and 100 cm^{-3} over ocean. For ice clouds, the particle size is specified from a temperature dependent relationship that is based upon an analysis of aircraft observations (Donner et al. 1997). Clouds are assumed to randomly overlap, an assumption which is tolerable for a model with only 18 vertical levels. The model's radiation budget is tuned so that the long-term global and annual mean outgoing longwave and absorbed solar radiation are equal and close to observed. This is accomplished primarily through adjustments to the critical radius for the onset of raindrop formation from liquid clouds (a value of $7.0 \mu\text{m}$ is used) and to the specified precipitation efficiency for deep convection in RAS.

4) TURBULENCE AND SURFACE FLUXES

For boundary layer and free atmospheric turbulence, the 2.5 order parameterization of Mellor and Yamada (1982) is used. To prevent the decoupling of the surface from the atmosphere and the resulting excessive cooling of the winter land surface temperatures (Derbyshire 1999), a minimum bound on the vertical diffusion coefficients of $5 \text{ m}^2 \text{ s}^{-1}$ is imposed for the two lowest flux levels over land. The need for an artificial lower bound, in part, reflects the difficulty in simulating the intermittent turbulence regime of the very stable boundary layer, a common problem of atmospheric models with parameterized turbulence (Beljaars 1998).

Surface fluxes are computed using Monin-Obukhov similarity theory, given the atmospheric model's lowest level wind, temperature, and moisture and the surface roughness lengths, temperature, and humidity. To recognize the contribution to surface fluxes from sub-grid scale

wind fluctuations, a ‘gustiness’ component which is proportional to the surface buoyancy flux is added to the wind speed (Beljaars 1995). Oceanic roughness lengths for momentum, heat, and moisture are modified for low wind speed conditions (Beljaars 1995). On the stable side, a minimum bound of 10^{-5} is imposed on all drag coefficients.

5) GRAVITY WAVE DRAG

Orographic gravity wave drag, parameterized according to Pierrehumbert (1986) and Stern and Pierrehumbert (1988), occurs when the parameterized vertical momentum flux of vertically propagating orographic gravity waves exceeds a saturation flux profile that is based on the criteria for convective overturning. At low Froude number, the parameterization of the surface vertical momentum flux is based on linear theory, but for large Froude number, the parameterization incorporates nonlinear effects. The overall amplitude of the base flux and the Froude number threshold for nonlinear effects are parameters that have been tuned to improve the simulation of sea level pressure gradients and zonal mean wind.

c. Land model LM2

The land model LM2 is the Land Dynamics (LaD) model described in detail by Milly and Shmakin (2002; hereinafter MS02). At unglaciated land points, water may be stored in three lumped reservoirs: snow pack, soil water (representing the plant root zone), and ground water. Energy is stored as sensible heat in five soil layers and as latent heat of fusion in snow. Soil water and ground water are not allowed to freeze, regardless of temperature. Evapotranspiration from soil is limited by a non-water-stressed bulk stomatal resistance and a soil-water-stress function. Drainage of soil water to groundwater occurs when the water capacity of the root zone is

exceeded. Groundwater discharge to surface water is proportional to groundwater storage. Model parameters vary spatially as functions of mapped vegetation and soil types but are temporally invariant. Certain LaD-model parameter values were modified from those assigned by MS02 for coupling with AM2; these are described below.

Parameters affecting surface albedo (snow-free surface albedo, snow albedo, and snow-masking depth) were tuned on the basis of a comparison of model output with NASA Langley Surface Radiation Budget data analyses (Darnell et al. 1988, Gupta et al. 1992). Additionally, to improve albedo fields, three sparse-vegetation classes of Matthews (1983) were re-assigned so that only Matthews' 'desert' class remained as desert in the LaD model; the other three were re-defined as LaD-model grassland.

When the LaD model was first run as LM2 coupled to AM2, computed values of evaporation from land were generally smaller than expected for the AM2 precipitation and surface net radiation. To remedy this bias, the non-water-stressed values of bulk stomatal resistance were reduced globally in LM2 by a factor of 5 from the values previously determined by stand-alone tuning of the LaD model (MS02). The magnitude of this reduction was chosen to produce rates of evaporation having relations to precipitation and surface net radiation consistent with the semi-empirical relation of Budyko (1974). The necessity for such a large parameter adjustment was unexpected and is under investigation. Discrepancies between stand-alone and coupled tuning of the LaD model may be related to fundamental problems in the stand-alone tuning strategy, which does not permit atmospheric feedbacks, and/or a tendency for AM2 to promote excessively cool, moist atmospheric conditions near the surface, which would suppress evaporation.

The heat capacity of soil was reduced globally by a factor of 4 in order to compensate for

systematic model errors that lead to an understandable bias in the amplitude of the surface diurnal temperature range. In humid regions, the model assumption of an isothermal surface (vegetation canopy and soil surface at a common temperature) promotes excessive sensible heat flux into the ground. In arid regions, the model use of an average soil wetness leads to overestimation of the soil heat capacity and thermal conductivity. Both of these problems were ameliorated by the global adjustment of heat capacity to match the Climate Research Unit (CRU) observations of near-surface atmospheric diurnal temperature range (New et al. 1999) to that simulated by AM2/LM2. The need to adjust the heat capacity was not unexpected. MS02 had neither analyzed nor tuned the diurnal temperature range, and mean water and energy balances, upon which they focused, are very insensitive to soil heat capacity.

Soil layers thicknesses were changed from the original values to (top to bottom) 0.02, 0.04, 0.09, 0.35, and 1 m. The purpose of this change was to thicken the top layer by a factor of 4, so as to suppress numerical problems introduced when the heat capacity was decreased.

d. Boundary conditions and integrations performed

The standard integration described in this study uses the observationally-based AMIP II SST and sea-ice prescriptions (Gates et al. 1999). The period of integration is from 1 January 1979 to 1 March 1996. The integration was initialized from another “spun up” integration of the model with slightly different boundary conditions and forcing from the AMIP prescription. The model output from this integration was submitted to the PCMDI in the Autumn of 2002. A monthly climatology was formed from this integration for the years 1979 through 1995 and was used to compare to observations in section 3a and section 4.

A second set of integrations discussed below is a 10-member ensemble of 50-year integrations, from January 1951 to December 2000, that uses another SST and sea-ice data prescription developed by J. Hurrell at NCAR (personal communication). The data from these integrations are used in the analysis of variability related to ENSO (sections 3b1 and 3b2) and the Northern Annular Mode (section 3b3).

3. Simulation characteristics

a. Model climatology

1) GENERAL CIRCULATION

Figure 1 shows the difference in annual- and zonal-mean temperature between the long-term mean of the AMIP II integration of AM2/LM2 and a 50-year climatology from the National Center for Environmental Prediction (NCEP) reanalysis (Kalnay et al. 1996). The model exhibits a cold troposphere and warm stratosphere bias throughout the year; typical errors in seasonal mean temperatures are 2 K and 4 K for tropospheric and stratospheric temperatures, respectively. The stratospheric warm bias at 50°N, with amplitudes as large as 8 K, is a problem that has shown considerable improvement in more recent versions of the model (~2 K). The model displays a high latitude Southern Hemisphere cold bias from 100 to 500 hPa that is common to many climate models; however, the magnitude of the error in AM2/LM2 is smaller than other models. Both the NCEP and European Centre for Medium-Range Weather Forecasts reanalysis (ECMWF) (Gibson et al. 1997) indicate zonal mean 200 hPa December-January-February (DJF) temperatures of about 225-230 K at 60°S to 90°S, whereas AM2/LM2 gives temperatures of 220-225 K for this region (215-220 K in more recent versions). In contrast, the median AMIP II model has tempera-

tures of about 211 K (P. Gleckler, personal communication). Reasons for this reduced cold bias of 200 hPa temperature are unclear.

The cold bias throughout most of the lower troposphere that is evident in Figure 1 extends to the land surface, as can be seen in the annual-mean 2 m surface air temperature error with respect to the CRU climatology (Fig. 2). Although the annual-mean plot is fairly representative of the full seasonal cycle, over the Northern Hemisphere a warm bias in boreal summer partially offsets winter cold biases. This is illustrated for North America in Figure 3; the warm bias in the southern United States corresponds to a mean temperature of 303 K or 30°C.

Figure 4 displays the annual and zonal-mean zonal winds from AM2/LM2, NCEP reanalysis, and the difference. Features which persist throughout the seasonal cycle include a westerly bias in the tropical middle troposphere and a weak Northern Hemisphere upper troposphere westerly jet. The middle and lower troposphere westerly jets tend to be equatorward shifted in both hemispheres; in the Southern Hemisphere this error is particularly sensitive to numerical details of the dynamical core. As for temperature, the largest wind errors are concentrated in the top levels of the model. Typical error amplitudes are 2 and 5 m s⁻¹ in the troposphere and stratosphere, respectively.

Figure 5 displays the long-term annual- and zonal- mean zonal windstress over the ocean for AM2/LM2 and three observational based datasets (see caption for details). Although there is a large spread among the observational datasets, robust biases are apparent: the AM2/LM2 surface wind stress amplitude is approximately 30% too large in both the subtropics and the extratropics, and the extratropical pattern displays a distinct equatorward shift that is most pronounced in the Northern Hemisphere. Given the sensitivity of the ocean to wind stress, this equatorward shift

represents a serious problem; in the region of 30°N to 60°N, AM2/LM2's simulation is outside the eightieth percentile range of the AMIP II models (P. Gleckler, personal communication).

Figure 6 illustrates the long-term mean Northern Hemisphere DJF sea level pressure (SLP) for AM2/LM2, the NCEP reanalysis, and the difference. The equatorward shift of the surface circulation pointed out for the annual-mean wind stress (Fig. 5) is particularly evident in the North Atlantic. Other biases are a somewhat weak Aleutian low, an excessively strong Icelandic low, and a high pressure bias of 8 to 10 hPa over the Arctic. This bias pattern is accompanied by anomalous easterlies in northwest Russia which contribute to the enhanced cold bias in that region (Fig. 2). The Arctic high-pressure bias and the low pressure error pattern at lower latitudes are reminiscent of an annular-mode circulation pattern (section 3b3). This bias pattern is common to many models (Fig.2 of Walsh et al. 2002) and in AM2/LM2 its magnitude has been reduced by weakening the damping at the top level of the model, which induces an annular-mode response that extends to the surface.

Figure 7 displays the departure from zonal mean of the 500 hPa DJF geopotential height, a useful metric of the model's ability to produce a realistic planetary wave pattern. Typical errors are on the order of 20 to 50 m and the error pattern is anticorrelated with the total field over the North Atlantic and North America, indicating a wind field that is too zonal. Particularly prominent is the weak Hudson Bay low. The excessive zonality is also evident in the 200 hPa wind pattern in the North Atlantic whose jet axis has insufficient southwest-northeast orientation in comparison to NCEP reanalysis (not shown).

2) PRECIPITATION, RADIATION, CLOUDS, AND WATER VAPOR

Figure 8 compares the annual mean climatological precipitation for the model to the observational climatology of Xie and Arkin (1997), also known as CMAP. Although the correlation coefficient is high, 0.9, the root mean square error, 1 mm d^{-1} , is about 50% of the spatial standard deviation of the field, 2 mm d^{-1} . A prominent error is too much precipitation south of the equator to the east of Papua-New Guinea. This double-ITCZ occurs in all seasons except DJF. Additional tropical errors, which are confirmed by comparison to the Global Precipitation Climatology Project (GPCP) data (Huffman et al. 1997), include deficits of precipitation in and to the west of the Maritime continent and in the South and tropical Atlantic convergence zones. Precipitation excesses occur in the western Indian and northwest tropical Pacific oceans. Another error is too much summertime precipitation in Siberia, Alaska, and Northern Canada where the model simulates double the CMAP precipitation. The positive bias in summertime high latitude precipitation is also present in the annual mean and is common to many models (Fig. 13 of Walsh et al. 2002). However, on an annual mean basis there does not appear to be a bias in precipitation minus evaporation; outflows from rivers feeding the Arctic ocean are not systematically overestimated (not shown). The global mean precipitation is $\sim 0.3 \text{ mm d}^{-1}$ too high relative to the CMAP mean of 2.67 mm d^{-1} (Table 3).

Figures 9 and 10 compare the long-term annual mean outgoing longwave radiation (OLR) and net shortwave absorbed (SWAbs) from AM2/LM2 to the observations of the Earth Radiation Budget Experiment (ERBE, Barkstrom et al. 1989). Root mean square errors are about 9 W m^{-2} for OLR and 12 W m^{-2} for SWAbs. Within the tropics, the pattern of errors is closely matches that of the precipitation errors, suggesting that improvements in the simulation of precipitation would

be accompanied by improvements in the radiation fields. Outside of the tropics, a prominent overestimate of SWAbs of about 10-20 W m⁻² occurs at nearly all longitudes of the southern ocean at about 60°S. The error, common to many models, occurs in the open ocean areas adjacent to the sea ice margin. Through comparison to data from the International Satellite Cloud Climatology Project (ISCCP, Rossow and Schiffer 1999), this error appears to be due to an underestimate of midlevel topped clouds. The amount of SWAbs over the Sahara is overestimated by up to 30 W m⁻² because LM2 assumes a single albedo for all deserts whereas the Sahara is considerably brighter than other deserts.

Although the clouds have been tuned to reproduce the global annual mean top of atmosphere (TOA) radiation budget, the surface radiation budget is somewhat independent. Both the estimates of the Global Energy and Water Experiment (GEWEX) (Stackhouse et al. 2003) and the Goddard Institute for Space Studies (GISS) (Zhang et al. 2003) indicate that the shortwave absorbed at the surface is a few W m⁻² too low (Table 3). The low bias in net shortwave absorbed results from the excess shortwave cloud forcing, which is the difference between clear sky and all-sky or total shortwave fluxes, outweighing the positive bias in clear-sky net shortwave absorbed at the surface. It is interesting to note that compared to integrations of AM2/LM2 without the specified three dimensional monthly climatology of aerosols, the SWAbs at the SFC is reduced by 4.7 W m⁻² while the longwave cooling of the surface is reduced by only 0.6 W m⁻². With regard to the surface longwave budget, it appears, relative to the two observational estimates, that AM2/LM2 overestimates the longwave cooling by 5 to 10 W m⁻², although under clear skies there is less bias.

With regard to the turbulent surface fluxes, the model overestimates the Kiehl and Trenberth (1997) estimate of evaporation by 8 W m⁻² and underestimates the sensible heat flux by 4 W

m^{-2} . Note that the sum of the Kiehl and Trenberth (1997) turbulent heat fluxes, 102 W m^{-2} , is lower than either the GEWEX or GISS estimates of the surface net radiation, about 115 W m^{-2} , by 10 to 15 W m^{-2} . Because the surface energy budget should sum to zero, this difference indicates significant remaining uncertainties in the surface energy budget. This suggests that the model's turbulent heat fluxes are not inconsistent with observations, and indeed the model's values lie within the range of observational estimates quoted in Table 1 of Kiehl and Trenberth (1997).

Figure 11 compares AM2/LM2's annual mean total cloud amount to the satellites estimates of ISCCP. The data used is the D2 adjusted monthly mean total cloud amounts (Rossow and Schiffer 1999) and the model and observations are sampled only from snow free and low surface elevation locations, due to the known problems in retrieving cloud amounts from satellites when snow or ice is on the surface and in mountainous terrains. Overall the comparison is good, with the model producing marine stratocumulus in the subtropical eastern oceans. Quantitatively, the model has a root-mean square error of 0.1 relative to both ISCCP and the surface observer climatology of Warren et al. (1986, 1988) (not shown). The globally averaged cloud cover of AM2/LM2 of 0.66 lies in between the ISCCP D2 value of 0.69 and the surface observers' value of 0.62. A noticeable problem of the model is the excessive wintertime cloudiness in northern Eurasia and North America; surface observers indicate about 0.5 cloud cover in these regions whereas AM2/LM2 has cloud cover in excess of 0.9. Much of this difference occurs in low cloudiness where the model has over 0.85 low cloudiness but the surface observers report low cloudiness under 0.25 (not shown). Averaged over the oceans, the liquid water path is 30% low relative to the two satellite estimates (Table 3) (Greenwald et al. 1993; Weng et al. 1997); this is accompanied by cloud drop effective radii which are too small. The model's simulation of ice water path cannot be assessed due to the lack of a reliable observational product with global coverage.

At the top of atmosphere, the magnitude of the global and annual averaged shortwave cloud forcing is overestimated by about 3 W m^{-2} but the longwave cloud forcing is underestimated by about 8 W m^{-2} (Table 3). Because the total OLR has been tuned to observations, the underestimate of the longwave cloud forcing indicates a similar significant error in the clear-sky OLR. Although the clear-sky sampling bias may contribute a few W m^{-2} to this difference (Hartmann and Doelling 1991), the model's clear-sky OLR is too low for probably two reasons. First, the troposphere has a cold bias relative to re-analyses (Fig. 1). Second, as shown in Figure 12, the model has a moist bias in the upper troposphere in comparison to estimates of upper tropospheric ($\sim 200\text{-}500 \text{ hPa}$) relative humidities from the TIROS Operational Vertical Sounder (TOVS) (Soden and Bretherton 1993). This moist bias is in excess of that due to the clear-sky sampling bias of the observations. This moist bias deduced from satellite observations is confirmed by both ECMWF and NCEP reanalyses which indicate a moist bias in both relative and absolute humidity in the middle tropical troposphere (not shown). The model's column water vapor (Table 3), a measure primarily of lower tropospheric water vapor, is too low, partially reflecting the model's cold bias as well as the fact that AM2/LM2's boundary layers are too shallow both for the convective boundary layer over land and for the marine stratocumulus-topped boundary layer (not shown).

b. Model variability

1) EXTRATROPICAL TELECONNECTIONS TO EL NIÑO/SOUTHERN OSCILLATION (ENSO)

The impact of ENSO-related SST anomalies on the extratropical circulation is illustrated in Figure 13, which displays the regression coefficients of 200 hPa height on the standardized NINO3 SST index for the DJF season. These charts have been constructed using NCEP reanalysis

data (lower panels) and the ensemble average of the 10 AM2/LM2 integrations (upper panels) for the 1951-2000 period (section 2d). The NINO3 index is defined as the areally averaged SST anomaly in the region 5°S-5°N, 150°W-90°W. The regression statistics in Figure 13 portray the typical 200 hPa height anomalies in response to a one-standard deviation SST forcing from the tropical Pacific.

The comparison between the upper and lower panels in this figure reveals considerable spatial similarities between the simulated and observed wavetrains emanating from the NINO3 region to the Southern Oceans and the eastern North Pacific/North American sector. The magnitude of the model anomalies in the eastern North Pacific and Canada is smaller than that of their observed counterparts. In this context, it is also noteworthy that the level of model variability, as measured by the temporal standard deviation of the simulated DJF 200 hPa height (not shown), is also lower than its observed counterpart. Considerable differences are discernible between the model and observed patterns over the Northwest Pacific and East Asia. One of the factors contributing to these discrepancies between the model and observed signals are errors in the simulated precipitation anomalies in the equatorial Pacific. In comparison to GPCP anomalies (not shown), the model generates excessive drying immediately to the north of the primary positive precipitation anomaly over the central equatorial Pacific, during warm ENSO events. Also, the positive near-equatorial precipitation anomaly in the model extends too far west to the Indonesian Archipelago.

The capability of the model to reproduce the circulation anomalies observed in individual El Niño and La Niña events is now examined. For each of the prominent warm and cold events in the 1951-2000 period (e.g., see listing in Trenberth 1997), the anomaly patterns of DJF 200 hPa height were computed using the NCEP reanalysis and the ensemble mean of the 10 model integra-

tions. The spatial correlation coefficient, root mean square (rms) difference, and ratio between the spatial variances of the model and observed fields in the North Pacific/North American sector (20°-70°N, 60°-180°W) are displayed using a ‘Taylor’ diagram (Gates et al. 1999 and Taylor 2001) in Figure 14. In this diagram, each event is indicated by a dot and a label corresponding to the last two digits of the year; for instance, the statistics for the 1982/83 El Niño event are indicated using the label ‘82’. The spatial correlation coefficient between the simulated and observed anomalies exceeds the 0.5 level for five (1957, 1965, 1982, 1991 and 1997) out of the eight warm events, and two (1973 and 1988) out of seven cold events. The model and observed patterns exhibit almost zero correlation with each other in the two warm events of 1969 and 1987, as well as in over half of the cold events (1955, 1964, 1970 and 1975). With the exception of the unusually strong El Niño events of 1982 and 1997, the spatial variance of the model pattern is noticeably lower than that of the observations, indicating relatively weaker ensemble-mean responses to ENSO forcing for a majority of the events considered. Inspection of the Taylor diagram for the ten individual members of the ensemble (not shown) reveals that the spatial variance of these members is typically larger than that of the ensemble mean for a given event, and is therefore in better agreement, in this respect, with the observations than the ensemble-mean result. The Taylor diagram for individual samples further illustrates that, for those events with high spatial correlation between the ensemble-mean and observations (e.g. 1982 and 1997), the agreement between many model samples and the observations is also high.

2) TROPICAL TELECONNECTIONS TO ENSO

Ample observational and model evidence exists for the impact of ENSO on the Asian-Australian monsoons (Lau and Nath 2000). Warm ENSO episodes are generally accompanied by

below normal precipitation during the wet summer monsoons over the Indian subcontinent (IND) and northern Australia (AUS). Additionally, the dry winter monsoon over southeast Asia (SEA) weakens in El Niño events resulting in above average rainfall amounts. The polarity of these anomalies tends to reverse during cold events.

The simulation of these ENSO-monsoon relationships by AM2/LM2 has been evaluated by examining the model's 10-member ensemble mean precipitation anomalies in the above-mentioned regions for each monsoon season in the 1951-2000 period. The covariability between the model's precipitation anomalies in these monsoon regions and the NINO3 SST anomalies is illustrated in the upper panels of Figure 15. The simulated precipitation anomalies in IND and AUS during the local summer season are negatively correlated with NINO3 SST anomalies, and the wintertime rainfall in SEA exhibits a positive correlation with the ENSO forcing. Many of the outstanding ENSO episodes (colored dots and squares) are accompanied by notable simulated rainfall perturbations simulated in the regions considered. The correlation coefficients between monsoon precipitation amounts in the AM2/LM2 model runs and the NINO3 index, as indicated in the upper right corner of individual panels, may be compared with those deduced from GPCP observational estimates (lower panels of Fig. 15). The noticeably weaker correlations between the observed Indian rainfall and the NINO3 index (lower left panel) reflect the much diminished Indian monsoon - ENSO relationships during the recent decades covered by the GPCP dataset (Kumar et al. 1999). The correlation coefficients between the observed rainfall anomalies and the NINO3 index for the outstanding ENSO episodes (shown above the lower panels without parenthesis) are based on only five events, and are hence subject to considerable sampling fluctuations.

3) NORTHERN ANNULAR MODE

Apart from ENSO, the dominant pattern of interannual climate variability is associated with the annular modes of the extratropical atmospheric circulation field. Shown in Figure 16 are maps of the SLP and temperature fields associated with the observed (left panel) and simulated (right panel) Northern Annular Mode (NAM, also referred to as the Arctic Oscillation). The NAM is defined as the first Empirical Orthogonal Function (EOF) of SLP over the domain from 20°N to 90°N. The contours indicate the SLP changes associated with a 1 hPa increase of a NAM index, defined as the difference in SLP between the Arctic and midlatitude extrema of the EOF pattern multiplied by the EOF time series, which yields an index in units of hPa. The model has a realistic simulation of the NAM, although the relative amplitude of the North Atlantic center is weaker in the model than in the observations. The color shading indicates the near surface air temperature anomalies associated with a 1 hPa increase in the NAM index. Consistent with the observations, a positive phase of the simulated NAM is associated with a quadrupole field of temperature anomalies: warm anomalies over southeastern North America and northern Eurasia, and cold anomalies over northeastern North America and northern Africa through the Middle East. The primary discrepancy between the simulated and observed temperature fields related to the NAM occurs over northwestern North America, with larger cold anomalies in the model than observed. This is consistent with the differences in the simulated and observed SLP anomaly fields over that region.

4) TROPICAL TRANSIENT ACTIVITY

Transient activity in the tropics is evaluated by examination of 2 phenomena: tropical cyclones and the Madden-Julian Oscillation (MJO).

Tropical cyclones in AM2/LM2 are detected using the algorithm of Vitart et al. (1997) and compared to the National Climatic Data Center's global tropical cyclone position data (Neumann et al. 1999). Figure 17 displays genesis location frequencies for the years 1979-1995. AM2/LM2 underestimates the number of storms quite significantly, particularly in the Atlantic and Eastern Pacific, where there are almost no storms at all. Particularly noticeable is that the model fails to simulate the minimum of cyclone genesis at the equator. The seasonal cycle of storms is also quite poor (not shown); for example, in the Northwest Pacific basin AM2/LM2 has a peak number of storms in November, 2 months after the observed peak. One might reasonably question whether a global model should be able to simulate tropical cyclones which in nature can be significantly smaller than the grid resolution. Indeed, a version of AM2/LM2 with 1° resolution simulates twice the number of cyclones as the control model. Note, however, that this measure of tropical variability can be highly sensitive to model changes, even for a fixed resolution. For example, a very early version of the AM2/LM2 model had a considerably larger number of tropical cyclones and a better tropical cyclone seasonal cycle.

An assessment of the MJO is made by examining the structure and behaviour of intraseasonal variability, defined as variability with timescales between 30 and 90 days. Figure 18 displays the wave frequency spectra for the 30 to 90 day band-passed 200 hPa zonal wind. Spectral peaks in the intraseasonal range are evident in the NCEP reanalyses, with the observed maxima primarily in the 40 to 60 day range. AM2/LM2 shows weaker peaks in the vicinity of 40 to 60 days with some additional variance at timescales longer than 60 days, implying a somewhat slower propagation speed. The first EOF of band-passed CMAP observed precipitation explains over 10% of the total variance and shows two coherent regions of intraseasonal variability centered near the equator at approximately 85°E and 165°E (Fig. 19, bottom panel). Of note is the

fairly broad meridional extent of this intraseasonal mode on both sides of the equator. In contrast, the first EOF of intraseasonal variance in the AM2/LM2 explains only about 4% of the variance and appears to be equatorially confined with a maximum amplitude in the western Pacific around 160°E (Fig. 19, top panel). To the extent that the first EOF is a proxy for the general characteristics of intraseasonal variance, the AM2/LM2 is particularly deficient in the Indian Ocean south of the Bay of Bengal when compared to CMAP. Waliser et al. (2002) indicate that this is a common deficiency of GCMs.

4. Comparison of AM2/LM2 climatology to other models

It is of general interest to compare the skill of AM2/LM2 in reproducing observed climate with that of other models. To do so, Taylor diagrams (see legend of Fig. 14 for a detailed explanation of these diagrams) have been calculated for eight variables using AM2/LM2, two previous GFDL models, and four non-GFDL models (Fig. 20). The first row of Fig. 20 displays variables associated with surface climate, including boreal winter ocean-only SLP, boreal summer Northern Hemisphere land-only surface air temperatures, and annual mean ocean-only zonal wind stress. The second row displays variables related to hydrology: annual mean tropical precipitation, short-wave cloud forcing, and total cloud amount. The last row displays variables related to upper tropospheric circulation: the boreal winter 200 hPa eddy geopotential in the Northern Hemisphere and the 200 hPa zonal wind.

The previous GFDL models include the GFDL climate model recoded into FMS software which is known locally as the Manabe Climate Model (MCM) (Delworth et al. 2002) and the model developed by the GFDL's former experimental prediction group (DERF) (Stern and Miyakoda 1995). The data from models outside of GFDL were acquired from the archive maintained at

the PCMDI and represents their official submission to AMIP II. The outside models include the CCM3.5 of the National Center for Atmospheric Research, ECHAM4 of the Max Planck Institute, the ECMWF model CY18R5, and HadAM3 from the United Kingdom's Meteorological Office. The experimental data produced by the non-GFDL models were submitted to PCMDI in either 1998 or 1999 (see <http://www-pcmdi.llnl.gov/amip/STATUS/incoming.html> for documentation).

Broadly speaking, the figure indicates that AM2/LM2 produces a model climate better than that of the previous GFDL models, particularly in variables related to hydrology and clouds. The variables related to 200 hPa circulation are more equivocal; the placement of the data points representing AM2/LM2 well within the unit arc circle indicates that the spatial variance of the model field is underestimated relative to observations. In the case of the eddy geopotential, this result is consistent with that shown in Fig. 7. The quality of AM2/LM2's climate is comparable to that produced by the non-GFDL models. In some variables (SLP and total cloud amount), the AM2/LM2 model is at the front rank, but for other variables AM2/LM2 is slightly worse (200 hPa zonal wind). It is important to state two caveats of this model comparison: these Taylor diagrams compare only model climatologies, no results are shown for different aspects of model variability; and the performance of non-GFDL models may have improved in the years since their submission of data to AMIP II.

5. Future work

A new global atmosphere and land model AM2/LM2 developed at GFDL has been presented and the model evaluated using a simulation in which the model is forced with observed SSTs and sea ice. In this final section, the suitability of AM2/LM2 for coupling with an ocean and

future plans for global atmosphere and land modeling at GFDL are discussed.

The ultimate goal for this work is to successfully couple AM2/LM2 to an ocean model without flux adjustments. This work is ongoing, but a preliminary indication of the ability of AM2/LM2 to couple with an ocean model is given by estimates of the implied poleward oceanic heat transport for the Atlantic, Indo-Pacific, and world ocean basins (Fig. 21). For comparison, observational based estimates of oceanic heat transport derived from atmospheric data (Trenberth and Caron 2001) and oceanic data (MacDonald 1998) are also shown. Due to AM2/LM2's imbalance of net radiation at the top of the atmosphere and the neglect of some minor surface heat flux terms in the analysis, a net flux imbalance across the air-sea interface exists which is accounted for by subtracting 1.8 W m^{-2} from each ocean grid box before computing the model's implied heat transport. Note that it is unlikely that this global adjustment affects the results significantly as the experience of tuning AM2/LM2 to remove these small imbalances in the net radiation make very tiny differences (< 0.1 petawatts (10^{15} W)) in the derived transports. AM2/LM2's implied oceanic heat transport is in reasonable agreement with the observed estimates in the Atlantic basin, except for the tropical South Atlantic, where the model's implied oceanic heat transport is too low. In the North Atlantic, AM2/LM2's simulation represents a significant improvement over that implied by the atmosphere component of the older GFDL R30 climate model (Delworth et al. 2002) which had too small implied poleward heat transport (0.7 petawatts at 15°N , not shown). In the Indo-Pacific basin, the model's implied oceanic heat transport has a positive bias relative to both sets of observed estimates, and exceeds Trenberth and Caron's 1 standard error limit from 10°S to 60°N . This indicates that in the North Pacific the model atmosphere removes heat from the ocean at a greater rate than is supported by either set of observations.

GFDL GAMDT

AM2/LM2 is undergoing constant development; the version of the model described in this paper corresponds to that current during the summer of 2002. Noteworthy incremental changes since then include the incorporation of the piecewise parabolic form of the finite volume vertical advection of tracers which has greatly improved the simulation of stratospheric water vapor, and the inclusion of a simple form of cumulus momentum transport which has lessened the double-ITCZ problem.

The development of the next version of the atmospheric model, AM3, is well under way and contains four main thrusts. First, RAS will be replaced by a more advanced convection scheme (Donner et al. 2001) which includes representations of vertical velocities and microphysics in cumulus updrafts and downdrafts, and parameterized mesoscale circulations. Second, the Mellor-Yamada turbulence scheme will be replaced by a parameterization based upon the work of Grenier and Bretherton (2001) and Lock et al. (2000). The new parameterization will include representation of the effects of condensation on vertical stability, an entrainment parameterization for the mixing between the boundary layer and the free troposphere, and a parameterization of the generation of turbulence by cloud top radiative cooling. Enhanced vertical resolution in the boundary layer will accompany this change. It is anticipated that this change will reduce the tendency for AM2/LM2 to produce too shallow boundary layers. Third, more vertical levels will be added at the top of the model to better simulate the stratosphere and its coupling with the troposphere. To do this, a new anisotropic orographic gravity wave scheme (Garner 2003) and a convectively generated gravity wave scheme (Alexander and Dunkerton 1999) will be added. Fourth, the model is being tested with prognostic chemistry and aerosol modules. A new land model LM3 is also under development.

Acknowledgments. Former GFDL director Jerry Mahlman is thanked for his encouragement and support of the Flexible Modeling System and current GFDL director Ants Leetmaa is thanked for his chartering of the Global Atmospheric Model Development Team. Internal reviews of the manuscript by Olivier Pauluis and Mike Winton are appreciated. Assistance regarding surface radiation budget data provided by Paul Stackhouse and Yuanchong Zhang is appreciated.

References

- Alexander, M.J. and T.J. Dunkerton, 1999: A spectral parameterization of mean-flow forcing due to breaking gravity waves. *J. Atmos. Sci.*, **56**, 4167-4182.
- Arakawa, A. and V. R. Lamb, 1977: Computational design of the basic dynamical processes of the UCLA general circulation model. *Methods in Computational Physics*, Vol. 17, J. Chang, Ed., Academic Press, 173-265.
- Barkstrom, B. R., E. Harrison, G. Smith, R. Green, J. Kibler, R. Cess, and the ERBE Science Team, 1989: Earth Radiation Budget Experiment (ERBE) archival and April 1985 results. *Bull. Amer. Met. Soc.*, **70**, 1254-1262.
- Beljaars, A. C. M., 1995: The parameterization of surface-fluxes in large-scale models under free convection. *Quart. J. Roy. Meteor. Soc.*, **121**, 255-270.
- Beljaars, A. C. M., 1998: Role of the boundary layer in a numerical weather prediction model, in *Clear and Cloudy Boundary Layers*, A. A. M. Holtslag, P. G. Duynkerke, and P. J. Jonker, Eds., Royal Netherlands Academy of Arts and Sciences, 287-304.

GFDL GAMDT

Budyko, M. I., 1974: *Climate and Life*. Academic, 508 pp.

CERSAT-IFREMER, 2002: Mean Wind Fields (MWF product), User manual. Volume 1: ERS-1, ERS-2, and NSCAT. C2-MUT-W-05-IF. Brest, France, 72 pp. (available at ftp://ftp.ifremer.fr/ifremer/cersat/documentation/gridded/mwf-ers/mwf_vol1.pdf)

Clough, S. A., M. J. Iacono and J-L. Moncet, 1992: Line-by-line calculations of atmospheric fluxes and cooling rates: Application to water vapor. *J. Geophys. Res.*, **97**, 15761-15785

Darnell, W. L., W. F. Staylor, S. K. Gupta, F. M. Denn, 1988: Estimation of surface insolation using sun-synchronous satellite data. *J. Clim.*, **1**, 820-836.

A. daSilva, A. C. Young, and S. Levitus, 1994. Atlas of surface marine data 1994. Volume 1: Algorithms and procedures. Technical Report #6, U.S. Department of Commerce, NOAA, NESDIS, 1994.

Delworth, T. L., R. J. Stouffer, K. W. Dixon, M. J. Spelman, T. R. Knutson, A. J. Broccoli, P. J. Kushner, and R. T. Wetherald, 2002: Review of simulations of climate variability and change with the GFDL R30 coupled climate model. *Clim. Dyn.*, **19**, 555-574.

Derbyshire, S. H., 1999: Boundary-layer decoupling over cold surfaces as a physical boundary instability. *Bound.-Layer Meteor.*, **90**, 297-325.

Donner, L. J., C. J. Seman, B. J. Soden, R. S. Hemler, J. C. Warren, J. Strom, and K.-N. Liou, 1997: Large-scale ice clouds in the GFDL SKYHI general circulation model. *J. Geophys. Res.*, **102**, 21745-21768.

- Donner, L. J., C. J. Seman, R. S. Hemler, and S. Fan, 2001: A cumulus parameterization including mass fluxes, convective vertical velocities, and mesoscale effects: thermodynamic and hydrological aspects in a general circulation model. *J. Clim.*, **14**, 3444-3463.
- Edwards, J. M. and and A. Slingo, 1996: Studies with a flexible new radiation code. I: Choosing a configuration for a large-scale model. *Quart. J. Roy. Meteor. Soc.*, **122**, 689-719.
- Fortuin, P. and H. Kelder, 1998: An ozone climatology based on ozonesonde and satellite measurements. *J. Geophys. Res.*, **103**, 31709-31734.
- Freidenreich, S. M., and V. Ramaswamy, 1999: A new multiple-band solar radiative parameterization for general circulation models. *J. Geophys. Res.*, **104**, 31389-31409.
- Fu, Q. and K.N. Liou, 1993: Parameterization of the radiative properties of cirrus clouds. *J. Atmos. Sci.*, **50**, 2008-2025.
- Gadd, A. J., 1978: A split explicit integration scheme for numerical weather prediction. *Quart. J. Roy. Meteor. Soc.*, **104**, 569-582.
- Garner, S. T., 2003: A topographic drag closure with analytically derived base flux. To be submitted to *J. Atmos. Sci.*.
- Gates, W.L., and Coauthors, 1999: An overview of the results of the Atmospheric Model Intercomparison Project (AMIP I). *Bull. Amer. Met. Soc.*, **80**, 29-55.
- Gibson, J. K., P. Kallberg, S. Uppala, A. Hernandez, A. Nomura, and E. Serrano, 1997: ERA description. ECMWF Reanalysis Project Rep. Series 1, European Centre for Medium-

Range Weather Forecasts, Reading, United Kingdom, 66 pp.

- Grenier, H. and C. S. Bretherton, 2001: A moist PBL parameterization for large-scale models and its application to subtropical cloud-topped marine boundary layers. *Mon. Wea. Rev.*, **129**, 357-377.
- Greenwald, T. J., G. L. Stephens, and T. H. Vonder Haar, 1993: A physical retrieval of cloud liquid water over the global oceans using Special Sensor Microwave/Imager (SSM/I) observations. *J. Geophys. Res.*, **98**, 18,471-18,488.
- Gupta, S. K., W. L. Darnell, and A. C. Wilber, 1992: A parameterization for longwave surface radiation from satellite data: Recent improvements. *J. Appl. Met.*, **31**, 1361-1367.
- Gupta, S. K., N. A. Ritchey, A. C. Wilber, C. H. Whitlock, G. G. Gibson, and P. W. Stackhouse Jr., 1999: A climatology of surface radiation budget derived from satellite data. *J. Clim.*, **12**, 2691-2710.
- Hamilton, K. P., R. J. Wilson, J. D. Mahlman, and L. Umscheid, 1995: Climatology of the SKYHI troposphere-stratosphere-mesosphere general circulation model. *J. Atmos. Sci.*, **52**, 5-43.
- Harrison, E. F., P. Minnis, B. R. Barkstrom, V. Ramanathan, R. C. Cess, and G. G. Gibson, 1990: Seasonal variation of cloud radiative forcing derived from the Earth Radiation Budget Experiment. *J. Geophys. Res.*, **95**, 18,687-18,703.
- Hartmann, D. L. and D. Doelling, 1991: On the net radiative effect of clouds. *J. Geophys. Res.*, **96**, 869-891.

- Haywood, J. M., V. Ramaswamy, and B. J. Soden, 1999: Tropospheric aerosol climate forcing in clear-sky satellite observations over the oceans. *Science*, *Science*, **283**, 1299-1303.
- Held, I., R. S. Hemler and V. Ramaswamy, 1993: Radiative-convective equilibrium with explicit two-dimensional moist convection. *J. Atmos. Sci.*, **50**, 3909-3927.
- Huffman, G. J., R. F. Adler, P. Arkin, A. Chang, R. Ferraro, A. Gruber, J. Janowiak, A. McNab, B. Rudolf, and U. Schneider, 1997: The Global Precipitation Climatology Project (GPCP) combined precipitation dataset. *Bull. Amer. Met. Soc.*, **78**, 5-20.
- Jakob, C. and S. A. Klein, 2000: A parameterization of the effects of cloud and precipitation overlap for use in general circulation models. *Quart. J. Roy. Meteor. Soc.*, **126**, 2525-2544.
- Jones, P. D., 1994: Hemispheric surface air temperature variations: a reanalysis and an update to 1993. *J. Clim.*, **7**, 1794-1802.
- Kalnay, E., and Coauthors, 1996: The NCEP/NCAR 40-year Reanalysis Project. *Bull. Amer. Met. Soc.*, **77**, 437-471.
- Kiehl, J. T. and K. E. Trenberth, 1997: Earth's annual global mean energy budget. *Bull. Amer. Met. Soc.*, **78**, 197-208.
- Kumar, K. K., B. Rajagopalan, and M. A. Cane, 1999: On the weakening relationship between Indian monsoon and ENSO. *Science*, **284**, 2156-2159.
- Kurihara, Y. and G. J. Tripoli, 1976: An iterative time integration scheme designed to preserve a low-frequency wave. *Mon. Wea. Rev.*, **104**, 761-764.

- Lau, N.-C., and M.J. Nath, 2000: Impact of ENSO on the variability of the Asian-Australian monsoons as simulated in GCM experiments. *J. Clim.*, **13**, 4287-4309.
- Lin, S.-J., W. C. Chao, Y. C. Sud, and G. K. Walker, 1994: A class of the van Leer-type transport schemes and its application to the moisture transport in a general circulation model. *Mon. Wea. Rev.*, **122**, 1575-1593.
- Lock, A. P., A. R. Brown, M. R. Bush, G. M. Martin, and R. N. B. Smith, 2000: A new boundary layer mixing scheme. Part I: Scheme description and single-column model tests. *Mon. Wea. Rev.*, **128**, 3187-3199.
- Lord, S. J. and A. Arakawa, 1980: Interaction of a cumulus cloud ensemble with the large-scale environment. Part II. *J. Atmos. Sci.*, **37**, 2677-2692.
- Macdonald, A. M., 1998: The global ocean circulation: a hydrographic estimate and regional analysis. *Progress in Oceanography*, **41**, 281-382.
- Matthews, E., 1983: Global vegetation and land use: new high-resolution data bases for climate studies. *J. Appl. Met.*, **22**, 474-487.
- Mellor, G.L. and T. Yamada, 1982: Development of a turbulent closure model for geophysical fluid problems. *Rev. Geophys. Space Phys.*, **20**, 851-875.
- Mesinger, F., 1977: Forward-backward scheme, and its use in a limited area model. *Contrib. Atmos. Phys.*, **50**, 186-199.
- Mesinger, F., Z. I. Janjic, S. Nickovic, D. Gavrilov and D. G. Deaven, 1988: The step-mountain

- coordinate: Model description and performance for cases of Alpine lee cyclogenesis and for a case of an Appalachian redevelopment. *Mon. Wea. Rev.*, **116**, 1493-1518.
- Milly, P. C. D., and A. B. Shmakin, 2002: Global modeling of land water and energy balances. Part I: The land dynamics (LaD) model. *J. Hydrometeor.*, **3**, 283-299.
- Moorthi, S. and M. J. Suarez, 1992: Relaxed Arakawa-Schubert: a parameterization of moist convection for general circulation models. *Mon. Wea. Rev.*, **120**, 978-1002.
- Moorthi, S. and M. J. Suarez, 1999: Documentation of version 2 of Relaxed Arakawa-Schubert cumulus parameterization with convective downdrafts. NOAA Technical Report NWS/NCEP 99-01, U.S. Dept. of Commerce, Camp Springs, MD.
- Neumann, C. J., B. R. Jarvinen, C. J. McAdie and J. D. Elms, 1999: Tropical cyclones of the North Atlantic ocean, 1871-1998. NCDC Historical Climatology Series, 6-2, 190 pp. (downloaded from <http://dss.ucar.edu/datasets/ds824.1/>)
- New, M., M. Hulme, and P. Jones, 1999: Representing twentieth-century space-time climate variability. Part I: Development of a 1961-90 mean monthly terrestrial climatology. *J. Clim.*, **12**, 829-856.
- Pierrehumbert, R. T., 1986. An essay on the parameterization of orographic gravity wave drag. Proceedings from ECMWF 1986 Seminar, Vol. I, 251-282.
- Ramachandran, S., V. Ramaswamy, G. L. Stenchikov, and A. Robock, 2000: Radiative impact of the Mount Pinatubo volcanic eruption: Lower stratospheric response. *J. Geophys. Res.*, **105**, 24409-24429.

- Ramaswamy, V., and M. M. Bowen, 1994: Effect of changes in radiatively active species upon the lower stratospheric temperatures. *J. Geophys. Res.*, **99**, 18909-18921.
- Ramaswamy, V., and M. D. Schwarzkopf, 2002: Effects of ozone and well-mixed gases on annual-mean stratospheric temperature trends. *Geophys. Res. Lett.*, **29**, 2064, 10.1029/2002GL015141.
- Randel, D. L. and co-authors, 1996: A new global water vapor dataset. *Bull. Amer. Met. Soc.*, **77**, 1233-1246.
- Rossow, W. B. and R. A. Schiffer, 1999: Advances in Understanding Clouds from ISCCP. *Bull. Amer. Met. Soc.*, **80**, 2261-2288.
- Rotstayn, L. D., 1997: A physically based scheme for the treatment of stratiform clouds and precipitation in large-scale models. I: Description and evaluation of microphysical processes. *Quart. J. Roy. Meteor. Soc.*, **123**, 1227-1282.
- Rotstayn, L. D., B. F. Ryan, and J. Katzfey, 2000: A scheme for calculation of the liquid fraction in mixed-phase clouds in large-scale models. *Mon. Wea. Rev.*, **128**, 1070-1088.
- Schwarzkopf, M. D., and V. Ramaswamy, 1999: Radiative effects of CH₄, N₂O, halocarbons and the foreign-broadened H₂O continuum: A GCM experiment. *J. Geophys. Res.*, **104**, 9467-9488.
- Shapiro, R., 1970: Smoothing, filtering and boundary effects. *Rev. Geophys. Space Phys.*, **8**, 359-387.

GFDL GAMDT

- Simmons, A. J. and D. M. Burridge, 1981: An energy and angular-momentum conserving vertical finite-difference scheme and hybrid vertical coordinates. *Mon. Wea. Rev.*, **109**, 758-766.
- Slingo, A., 1989: A GCM parameterization for the shortwave radiative properties of water clouds. *J. Atmos. Sci.*, **46**, 1419-1427.
- Soden, B. J. and F. P. Bretherton, 1993: Upper troposphere relative humidity from the GOES 6.7 μm channel: Method and climatology for July 1987. *J. Geophys. Res.*, **98**, 16,669-16,688.
- Stackhouse, P. W., Jr., S. J. Cox, S. K. Gupta, J. C. Mikovitz, and M. Chiacchio, 2003: The WCRP/GEWEX Surface Radiation Budget Data Set Release 2: A 1 degree resolution, 12 year flux climatology. in preparation.
- Stern, W. F. and R. T. Pierrehumbert, 1988: The impact of an orographic gravity wave drag parameterization on extended range predictions with a GCM. Preprints of the Eighth Conference on Numerical Weather Prediction, American Meteorological Society, Baltimore, 745-750.
- Stern, W. F. and K. Miyakoda, 1995: Feasibility of seasonal forecasts inferred from multiple GCM Simulations. *J. Clim.*, **8**, 1071-1085.
- Sud, Y. C. and G. K. Walker, 1999: Microphysics of clouds with the relaxed Arakawa-Schubert scheme (McRAS). Part I: Design and evaluation with GATE Phase III Data. *J. Atmos. Sci.*, **56**, 3196-3220.
- Taylor, J. P., J. M. Edwards, M. D. Glew, P. Hignett, and A. Slingo, 1996: Studies with a flexible new radiation code. Part II: Comparisons with aircraft short-wave observations. *Quart. J.*

- Roy. Meteor. Soc.*, **122**, 839-861.
- Taylor, K. E., 2001: Summarizing multiple aspects of model performance in a single diagram. *J. Geophys. Res.*, **106**, 7183-7192.
- Thompson, D. W. and J. M. Wallace, 1998: The arctic oscillation signature in the winter time geopotential height and temperature fields. *Geophys. Res. Lett.*, **25**, 1297-1300.
- Tiedtke, M., 1993: Representation of clouds in large-scale models. *Mon. Wea. Rev.*, **121**, 3040-3061.
- Trenberth, K. E., 1997: The definition of El Niño. *Bull. Amer. Met. Soc.*, **78**, 2771-2777.
- Trenberth, K. E., and J. M. Caron, 2001: Estimates of meridional atmosphere and ocean heat transports. *J. Clim.*, **14**, 3433-3443.
- Vitart, F., J. L. Anderson, and W. F. Stern, 1997: Simulation of interannual variability of tropical storm frequency in an ensemble of GCM integrations. *J. Clim.*, **10**, 745-760.
- Waliser, D. E., K. Jin, I.-S. Kang, W. F. Stern, S. D. Schubert, K.-M. Lau, M.-I. Lee, V. Krishnamurthy, A. Kitoh, G. A. Meehl, V. Y. Galin, V. Satyan, S. K. Mandke, G. Wu, Y. Liu and C.-K. Park, 2002: AGCM simulations of intraseasonal variability associated with the Asian summer monsoon. submitted to *Clim. Dyn.*
- Walsh, J. E., V. M. Kattsov, W. L. Chapman, V. Govorkova, and T. Pavlova, 2002: Comparison of Arctic climate simulations by uncoupled and coupled global models. *J. Clim.*, **15**, 1429-1446.

- Warren, S. G., C. J. Hahn, J. London, R. M. Chevin, and R. L. Jenne, 1986: Global distribution of total cloud cover and cloud type amounts over land. NCAR Technical Note TN-273+STR, Boulder, CO, 29 pp. + 200 maps. [Available from Carbon Dioxide Information Analysis Center, Oak Ridge, Tennessee.]
- Warren, S. G., C. J. Hahn, J. London, R. M. Chevin, and R. L. Jenne, 1988: Global distribution of total cloud cover and cloud type amounts over ocean. NCAR Technical Note TN-317+STR, Boulder, CO, 44 pp. + 170 maps. [Available from Carbon Dioxide Information Analysis Center, Oak Ridge, Tennessee.]
- Weng, F., N. C. Grody, R. Ferraro, A. Basist, and D. Forsyth, 1997: Cloud liquid water climatology from the Special Sensor Microwave/Imager. *J. Clim.*, **10**, 1086-1098.
- Woodruff, S. D., R. J. Slutz, R. L. Jenne and P. M. Steurer, 1987: A Comprehensive Ocean-Atmosphere Data Set. *Bull. Amer. Met. Soc.*, **68**, 1239-1239.
- Wyman, B.L., 1996: A step-mountain coordinate general circulation model: Description and validation of medium-range forecasts. *Mon. Wea. Rev.*, **124**, 102-121.
- Xie, P. and P. A. Arkin, 1997: Global precipitation: A 17-year monthly analysis based on gauge observations, satellite estimates, and numerical model outputs. *Bull. Amer. Met. Soc.*, **78**, 2539-2558.
- Zhang, Y.-C., W. B. Rossow, A. A. Lacis, V. Oinas, and M. I. Mishchenko, 2003: Calculation of radiative flux profiles from the surface to top-of-atmosphere based on ISCCP and other global datasets: Refinements of the radiative transfer model and the input data. in preparation for *J. Geophys. Res.*

Table captions

Table 1. Brief description of AM2/LM2 components.

Table 2. Coefficients a_k and b_k for calculation of interface level values. The coefficients are used in the Simmons-Burridge (1981) formula $p = a_k + b_k * p_s$, where p is pressure and p_s is surface pressure. The pressures p and geopotential heights z of interface levels using a scale height of 7.5 km and $p_s = 1000$ hPa are also shown.

Table 3. Selected global annual mean radiation budget and hydrologic quantities. Observational data sources are ERBE: Harrison et al. (1990); GEWEX: Stackhouse et al. (2003); GISS: Zhang et al. (2003); KT: Kiehl and Trenberth (1997); NVAP: Randel et al. (1996), GR: Greenwald et al. (1993); WG: Weng et al. (1997); ISCCP: Rossow and Schiffer (1999); SFC: Warren et al. (1986,1988); CMAP: Xie and Arkin (1997); GPCP: Huffman et al. (1997).

GFDL GAMDT

Component	Description
Dynamics	B-grid model, 2.5° lon by 2.0° lat 18 vertical levels with effective model top at about 40 km
Radiation	Diurnal cycle with full radiation calculation every 3 hours Effects of H ₂ O, CO ₂ , O ₃ , O ₂ , N ₂ O, CH ₄ , and 4 halocarbons included
<i>Longwave:</i>	Simplified Exchange Approximation (Schwarzkopf and Ramaswamy 1999) Clough et al. (1992) CKD 2.1 H ₂ O continuum parameterization
<i>Shortwave:</i>	Exponential Sum Fit with 18 bands (Freidenreich and Ramaswamy 1999) Liquid cloud radiative properties from Slingo (1989) Ice cloud radiative properties from Fu and Liou (1993)
<i>Aerosols:</i>	Prescribed monthly three-dimensional climatology from various chemical transport models. Species represented include sulfate, hydrophilic and hydrophobic carbon, dust, and sea salt.
Clouds	3 prognostic tracers: cloud liquid, cloud ice, and cloud fraction Cloud microphysics from Rotstayn (1997) Cloud macrophysics from Tiedtke (1993)
Convection	Relaxed Arakawa Schubert (Moorthi and Suarez 1992) Detrainment of cloud liquid, ice and fraction from convective updrafts into stratiform clouds
Vertical diffusion	Mellor-Yamada (1982) 2.5 order dry parameterization Surface fluxes from Monin-Obukhov similarity theory Gustiness enhancement to wind speed used in surface flux calculations (Beljaars 1995)
Gravity Wave Drag	Orographic drag from Stern and Pierrehumbert (1988)
Land Model	5 layer temperature model 11 soil and vegetation types Stomatal resistance Bucket hydrology and river routing

Table 1. Brief description of AM2/LM2 components.

GFDL GAMDT

k	a_k (Pa)	b_k	p (hPa)	z (km)
1	0	0	0	-
2	903.45	0	9	35.30
3	3474.8	0	35	25.20
4	7505.6	0	75	19.42
5	12787	0	128	15.43
6	19111	0	191	12.41
7	25340	0.0091759	263	10.03
8	26533	0.074216	340	8.10
9	26408	0.15638	420	6.50
10	25093	0.25235	503	5.15
11	22776	0.35821	586	4.01
12	19689	0.46961	666	3.04
13	16095	0.58189	743	2.23
14	12279	0.6902	813	1.55
15	8534.8	0.78957	875	1.00
16	5159.5	0.87501	927	0.57
17	2439.9	0.94163	966	0.26
18	642.68	0.98474	991	0.07
19	0	1	1000.00	0

Table 2. Coefficients a_k and b_k for calculation of interface level values. The coefficients are used in the Simmons-Burridge (1981) formula $p = a_k + b_k * p_s$, where p is pressure and p_s is surface pressure. The pressures p and geopotential heights z of interface levels using a scale height of 7.5 km and $p_s = 1000$ hPa are also shown.

GFDL GAMDT

Measure	Source	Observation	AM2/LM2
<i>Top of Atmosphere Radiation Budget ($W m^{-2}$)</i>			
Shortwave absorbed	ERBE	239.3	236.1
Outgoing longwave radiation	ERBE	234.5	236.9
Clear-sky shortwave absorbed	ERBE	287.7	288.1
Clear-sky outgoing longwave radiation	ERBE	265.6	259.6
Shortwave cloud forcing	ERBE	-48.4	-51.9
Longwave cloud forcing	ERBE	31.1	22.7
<i>Surface Energy Budget ($W m^{-2}$)</i>			
Shortwave absorbed	GEWEX/GISS	164.6/165.2	162.6
Net longwave	GEWEX/GISS	-47.1/-50.9	-57.1
Clear-sky shortwave absorbed	GEWEX/GISS	214.7/218.4	219.3
Clear-sky downward longwave	GEWEX/GISS	309.6/313.5	313.7
Shortwave cloud forcing	GEWEX/GISS	-50.1/-53.3	-56.7
Longwave down cloud forcing	GEWEX/GISS	35.6/31.1	25.2
Sensible heat flux	KT	24	20.7
Latent heat flux	KT	78	85.0
<i>Hydrologic Quantities</i>			
Column integrated water vapor ($kg m^{-2}$)	NVAP	24.5	23.7
Column integrated oceanic cloud liquid ($g m^{-2}$)	GR/WG	76.2/63.4	48.8
Column integrated cloud ice ($g m^{-2}$)	-	-	34.7
Total cloud amount (fraction)	ISCCP/SFC	0.69/0.62	0.66
Surface Precipitation ($mm d^{-1}$)	CMAP/GPCP	2.67/2.65	2.94

Table 3. Selected global annual mean radiation budget and hydrologic quantities. Observational data sources are ERBE: Harrison et al. (1990); GEWEX: Stackhouse et al. (2003); GISS: Zhang et al. (2003); KT: Kiehl and Trenberth (1997); NVAP: Randel et al. (1996), GR: Greenwald et al. (1993); WG: Weng et al. (1997); ISCCP: Rossow and Schiffer (1999); SFC: Warren et al. (1986,1988); CMAP: Xie and Arkin (1997); GPCP: Huffman et al. (1997).

Figure captions

Figure 1. Long-term annual and zonal mean temperature difference between NCEP/NCAR reanalysis climatology and AM2/LM2 (AM2/LM2 minus NCEP). Contour interval is 1 K.

Figure 2. Long-term annual mean 2 m temperature difference between CRU climatology and AM2/LM2 (AM2/LM2 minus CRU). Contour interval is 2 K.

Figure 3. Long-term mean 2 m temperature difference for North America between CRU climatology and AM2/LM2 (AM2/LM2 minus CRU) for DJF (top panel) and June-July-August (JJA) (bottom panel). Contour interval is 2 K.

Figure 4. Long-term annual and zonal mean zonal wind in m s^{-1} for (a) NCEP/NCAR reanalysis, (b) AM2/LM2, and (c) AM2/LM2 minus NCEP. Contour interval is 5 m s^{-1} in (a) and (b) and 2 m s^{-1} in (c).

Figure 5. Long-term annual and zonal mean zonal wind stress in Pa over the ocean for the ship-based climatology of COADS (blue) (daSilva et al. 1994; Woodruff et al. 1987), ECMWF reanalysis (red), the ERS satellite scatterometer (green) (CERSAT-IFREMER 2002), and AM2/LM2 (black). The sign convention is such that a positive stress indicates an easterly stress on the atmosphere and a westerly stress on the ocean.

Figure 6. Long-term Northern Hemisphere DJF mean SLP for (a) AM2/LM2, (b) NCEP/NCAR reanalysis, and (c) AM2/LM2 minus NCEP. Contour interval is 5 hPa for (a) and (b) and 2 hPa for (c); the zero contour is not plotted in (c). Note that regions with mean surface pressure below 750 hPa have been masked.

Figure 7. Long-term DJF mean departure of 500 hPa geopotential height from its zonal mean for (a) AM2/LM2, (b) NCEP/NCAR reanalysis climatology, and (c) AM2/LM2 minus NCEP. Contour interval is 25 m in (a) and (b) and 10 m in (c). Statistics at the bottom of (a) and (b) include the Northern Hemisphere mean and standard deviation. Statistics at the bottom of (c) include the difference in Northern Hemisphere means, the root mean square error, and the correlation coefficient.

Figure 8. Annual long-term mean precipitation in mm d^{-1} for (a) AM2/LM2, (b) CMAP observations, and (c) AM2/LM2 minus CMAP. Statistics at the bottom of (a) and (b) include the global mean and standard deviation. Statistics at the bottom of (c) include the difference in global means, the correlation coefficient, and the root mean square error.

Figure 9. Annual long-term mean outgoing longwave radiation (OLR) in W m^{-2} for (a) AM2/LM2, (b) ERBE observations, and (c) AM2/LM2 minus ERBE. Statistics at the bottom of (a) and (b) include the global mean and standard deviation. Statistics at the bottom of (c) include the difference in global means, the correlation coefficient, and the root mean square error. Note that the original ERBE observations have been scaled so they have a global annual mean of 237.2 W m^{-2} .

Figure 10. Annual long-term mean absorbed solar radiation (SWAbs) in W m^{-2} for (a) AM2/LM2, (b) ERBE observations, and (c) AM2/LM2 minus ERBE. Statistics at the bottom of (a) and (b) include the global mean and standard deviation. Statistics at the bottom of (c) include the difference in global means, the correlation coefficient, and the root mean square error. Note that the original ERBE observations have been scaled so they have a global annual mean of 237.2 W m^{-2} .

Figure 11. Annual long-term mean total cloud amount (fraction) for (a) AM2/LM2, (b) ISCCP

observations, and (c) AM2/LM2 minus ISCCP. Statistics at the bottom of (a) and (b) include the global mean and standard deviation. Statistics at the bottom of (c) include the difference in global means, the correlation coefficient, and the root mean square error. Regions with snow or ice at the surface or a surface elevation greater than 1000 m are not shaded in (a) or (b) as the ISCCP satellite estimates at these points are deemed unreliable.

Figure 12. Annual long-term mean upper tropospheric humidity in percent for (a) AM2/LM2, (b) TOVS observations, and (c) TOVS minus AM2/LM2. Statistics at the bottom of (a) and (b) indicate the global mean. Statistics at the bottom of (c) include the difference in global means, the correlation coefficient, and the root mean square error.

Figure 13. Distributions of the regression coefficients of 200 hPa height versus the standardized NINO3 SST index, as computed using the ensemble mean of the 10-member AMIP-style integrations with the AM2/LM2 (upper panels) and NCEP reanalyses (lower panels) for the December-January-February season of the 1951-2000 period. Results for the northern and southern extratropics are shown in the left and right panels, respectively. Contour interval is 5 m. The zero-contour is not plotted.

Figure 14. Taylor diagram depicting the relationships between the observed DJF 200 hPa height anomalies in the North Pacific / North American sector (20° - 70° N, 60° - 180° W) during selected ENSO events and the corresponding ensemble-mean patterns as simulated in the 10-member AMIP-style runs with the AM2/LM2. Results for individual warm and cold ENSO events are presented using red and blue dots, respectively. The two-digit label for each dot indicates the year of the event in question. The spatial correlation coefficient is given by the cosine of the angle between the abscissa and the straight line joining the origin and the dot representing the event of

interest; correlation values are given along the outer solid arc. The ratio between the simulated and observed spatial variances is given by the distance between the dot and origin; inner and outer solid arcs indicate ratios of 1 and 1.5, respectively. The root mean square (rms) difference between the simulated and observed pattern, as normalized by the spatial variance of the observed field, is given by the distance between the dot and the point with coordinates (1,0) in the diagram; inner and outer dotted arcs indicate normalized rms differences of 0.5 and 1, respectively.

Figure 15. Scatterplots of the precipitation anomalies in three monsoon regions [IND - Indian; AUS - northern Australia; SEA - southeast Asia; boundaries of these regions are depicted in Figure 3 of Lau and Nath (2000)] versus the NINO3 SST anomalies. The abscissa in all panels represents the standardized SST anomaly in the NINO3 region. The ordinate axis represents the standardized precipitation anomaly in IND during the JJA (left panels), and in SEA (middle panels) and AUS (right panels) during the DJF season. The upper panels are based on AM2/LM2 output for the 1951-2000 period. The lower panels show the observational estimates provided by GPCP for the shorter period of 1979-2000. In each panel, the anomalies of precipitation and NINO3 index for a given year are jointly depicted by a small dot or square. The outstanding warm and cold ENSO events are highlighted using colored dots and squares, respectively. The data for all remaining years are plotted using black dots. The correlation coefficient for the data entries in each panel is shown in the upper right corner of that panel. Correlation values based on all available years are given in parentheses. Correlation values based on the available warm and cold ENSO events only are given without parentheses.

Figure 16. Spatial pattern of the Northern Annular Mode (NAM) and associated temperature anomalies for the months of November through April. The NAM is defined by computing an

empirical orthogonal function (EOF) of SLP for all points north of 20°N. An NAM index is then calculated as the difference between the minimum and maximum of the spatial pattern of the first EOF multiplied by its associated time series, thereby yielding an index with units of hPa. The contours indicate the linear regression coefficients of SLP at each grid point versus an index of the NAM. The color shading indicates the linear regression coefficients on the NAM index of surface temperature at each grid point. The left panel displays analyses from observational data of SLP (Thompson and Wallace 1998), land surface air temperature (Jones 1994), and SST (Jones 1994). The right panel displays AM2/LM2 model results based upon one of the 50 year ARCs integrations. The model calculation uses surface air temperature over both land and ocean.

Figure 17. Frequency of tropical storm genesis for (a) observations and (b) AM2/LM2. Units are number of storms per year in a box of size 4° latitude by 5° longitude.

Figure 18. Wave frequency spectra of the variance of 30 to 90 day band-passed 200 hPa zonal wind, averaged for the period 1980 to 1995, for (a) AM2/LM2 and (b) NCEP reanalyses. Contour interval is 50 m²s⁻².

Figure 19. First EOF of 30 to 90 day band-passed precipitation, for the period 1980 to 1995, for (a) AM2/LM2 and (b) CMAP. Units are mm d⁻¹.

Figure 20. Taylor diagrams for selected variables comparing the skill of AM2/LM2 (red circle) in reproducing the observed climatology to that of older GFDL models (MCM and DERF, green and orange circles respectively) and other models participating in AMIP II (CCM3.5, ECHAM4, ECMWF, and HADAM3). Note that all non-GFDL models are plotted with a blue diamond to prevent unique identification. The selected variables include those associated with surface climate

GFDL GAMDT

(SLP, land surface air temperature, and oceanic wind stress, top row), hydrology and clouds (precipitation, shortwave cloud forcing, and total cloud amount, middle row), and upper tropospheric circulation (200 hPa eddy geopotential and zonal wind, bottom row). The observational sources for these data include the NCEP reanalyses for SLP and 200 hPa eddy geopotential and zonal wind, ECMWF reanalyses for oceanic wind stress, ERBE for cloud radiative forcing, ISCCP for total cloud amount, CMAP for precipitation and CRU for land surface air temperature. Beneath each variable name is an indication of the geographical domain and season used in the calculation.

Figure 21. Poleward oceanic heat transport in petawatts (10^{15} W) from observational based estimates and implied by AM2/LM2 (dark black line). The observed estimates are derived from atmospheric data (Trenberth and Caron 2001; red lines with dashed lines indicating plus or minus one standard error; based on NCEP-derived products) or oceanic data (MacDonald 1998; their Table 20; circles with error bars). Results are shown for the a) Atlantic, b) Indo-Pacific, and c) world ocean basins.

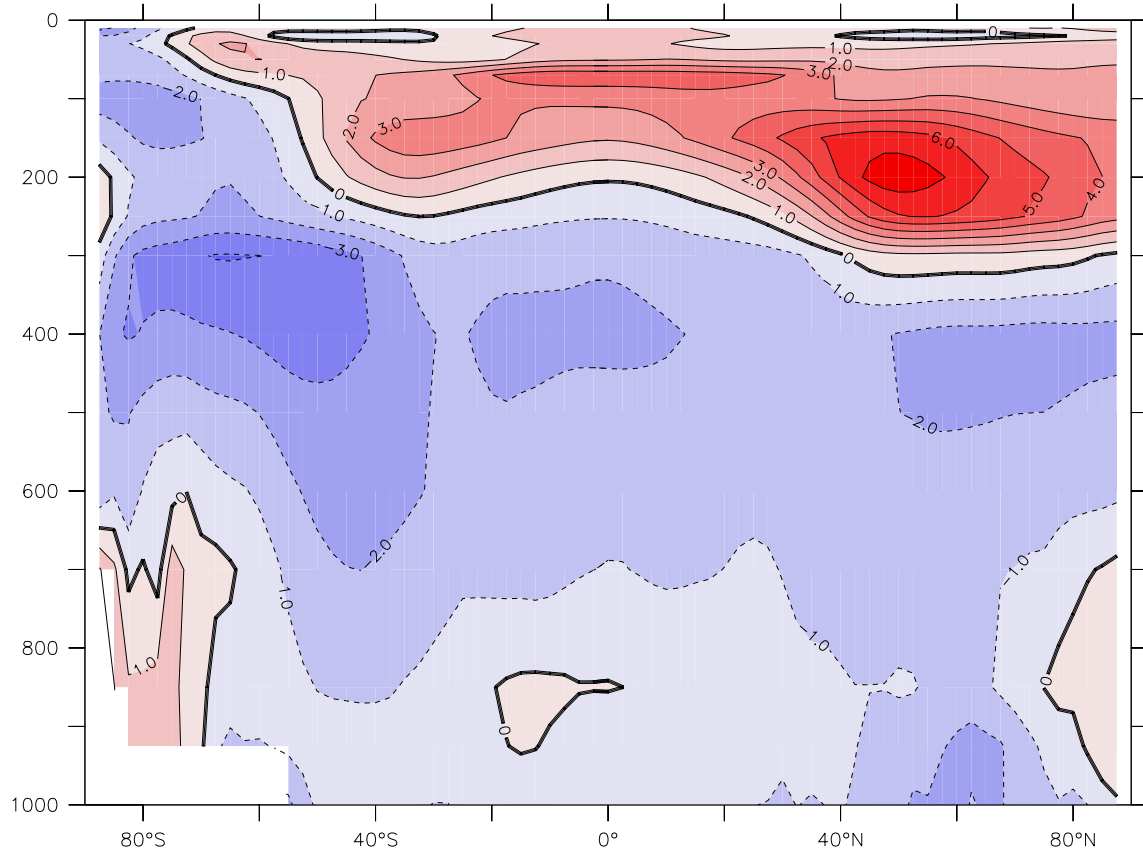


Figure 1. Long-term annual and zonal mean temperature difference between NCEP/NCAR reanalysis climatology and AM2/LM2 (AM2/LM2 minus NCEP). Contour interval is 1 K.

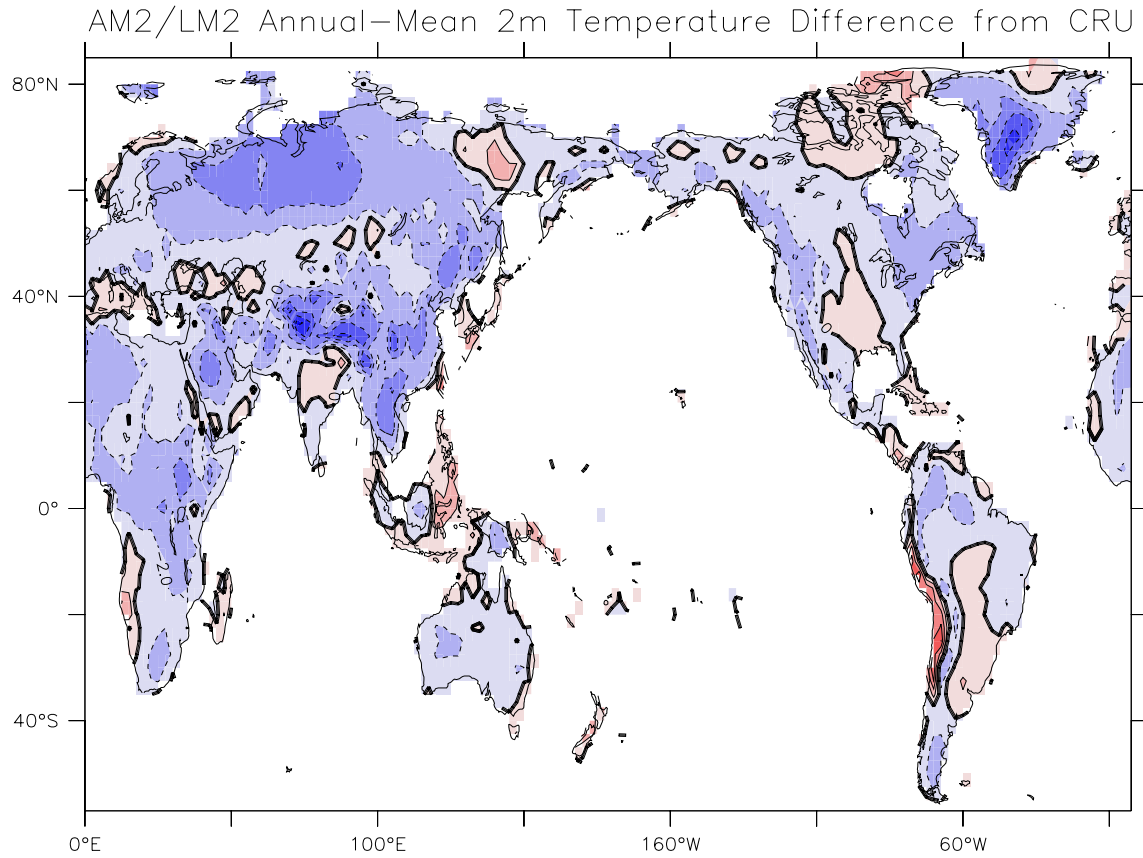
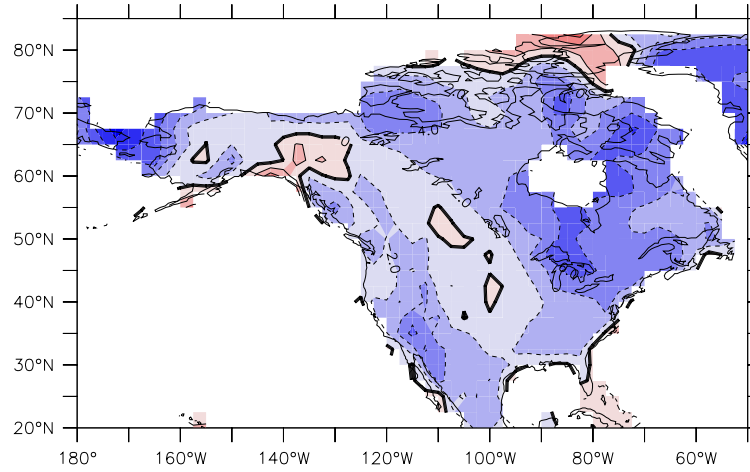
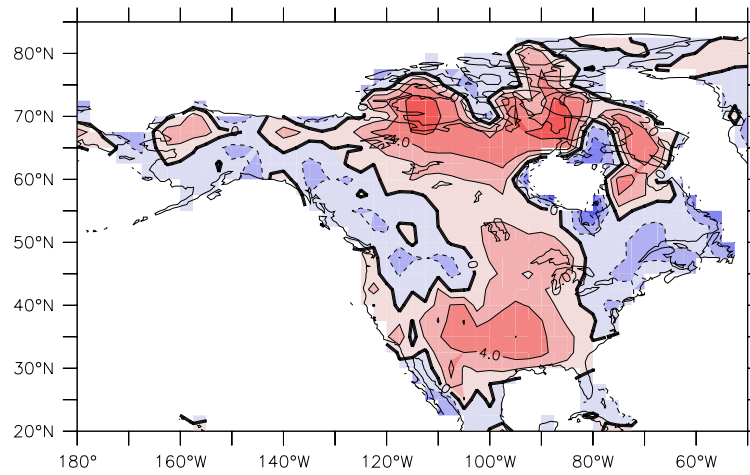


Figure 2. Long-term annual mean 2 m temperature difference between CRU climatology and AM2/LM2 (AM2/LM2 minus CRU). Contour interval is 2 K.

AM2/LM2 2m Temperature Difference from CRU



DJF



JJA

Figure 3. Long-term mean 2 m temperature difference for North America between CRU climatology and AM2/LM2 (AM2/LM2 minus CRU) for DJF (top panel) and June-July-August (JJA) (bottom panel). Contour interval is 2 K.

GFDL GAMDT

Zonal mean zonal wind, ann

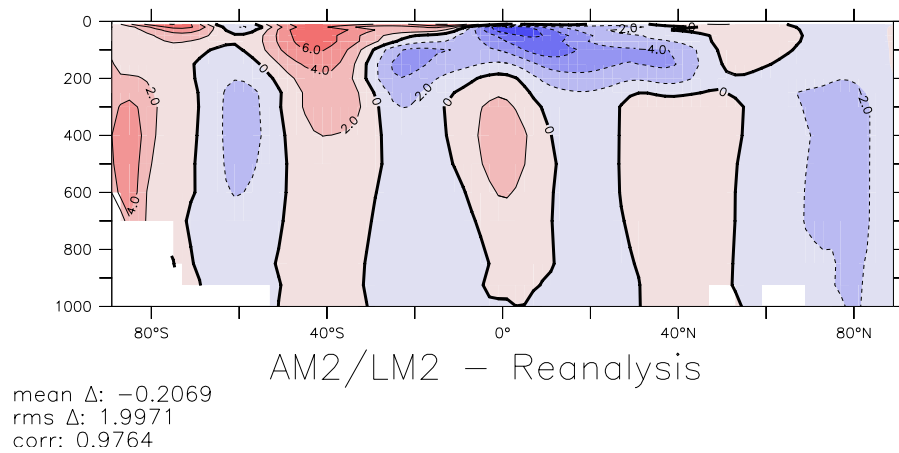
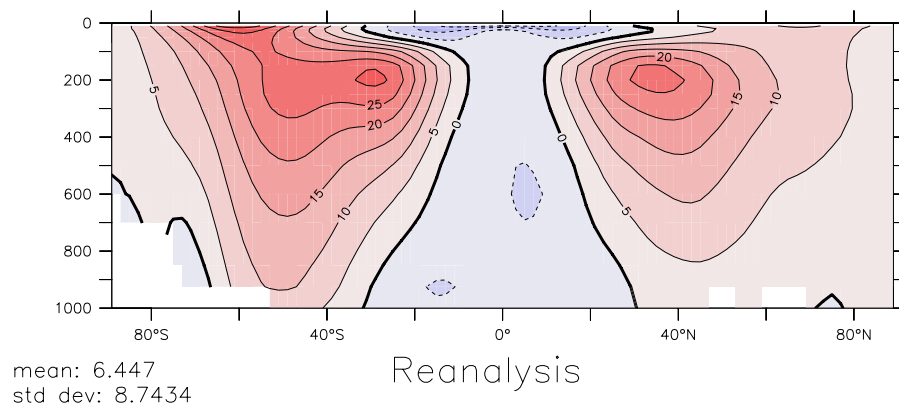
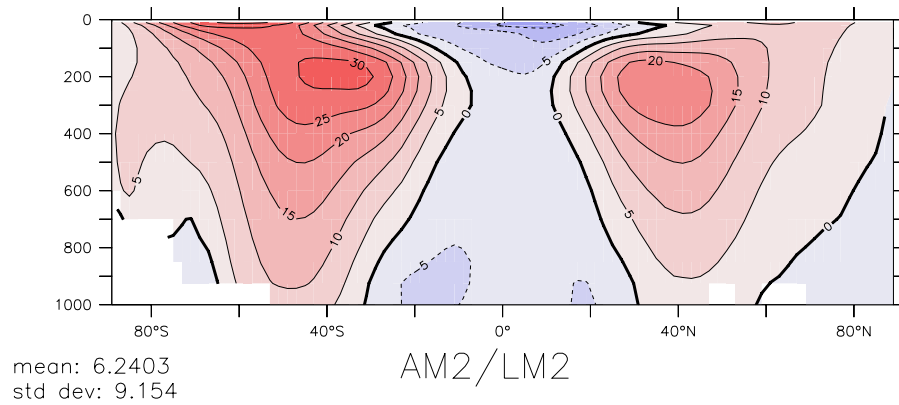


Figure 4. Long-term annual and zonal mean zonal wind in m s^{-1} for (a) NCEP/NCAR reanalysis, (b) AM2/LM2, and (c) AM2/LM2 minus NCEP. Contour interval is 5 m s^{-1} in (a) and (b) and 2 m s^{-1} in (c).

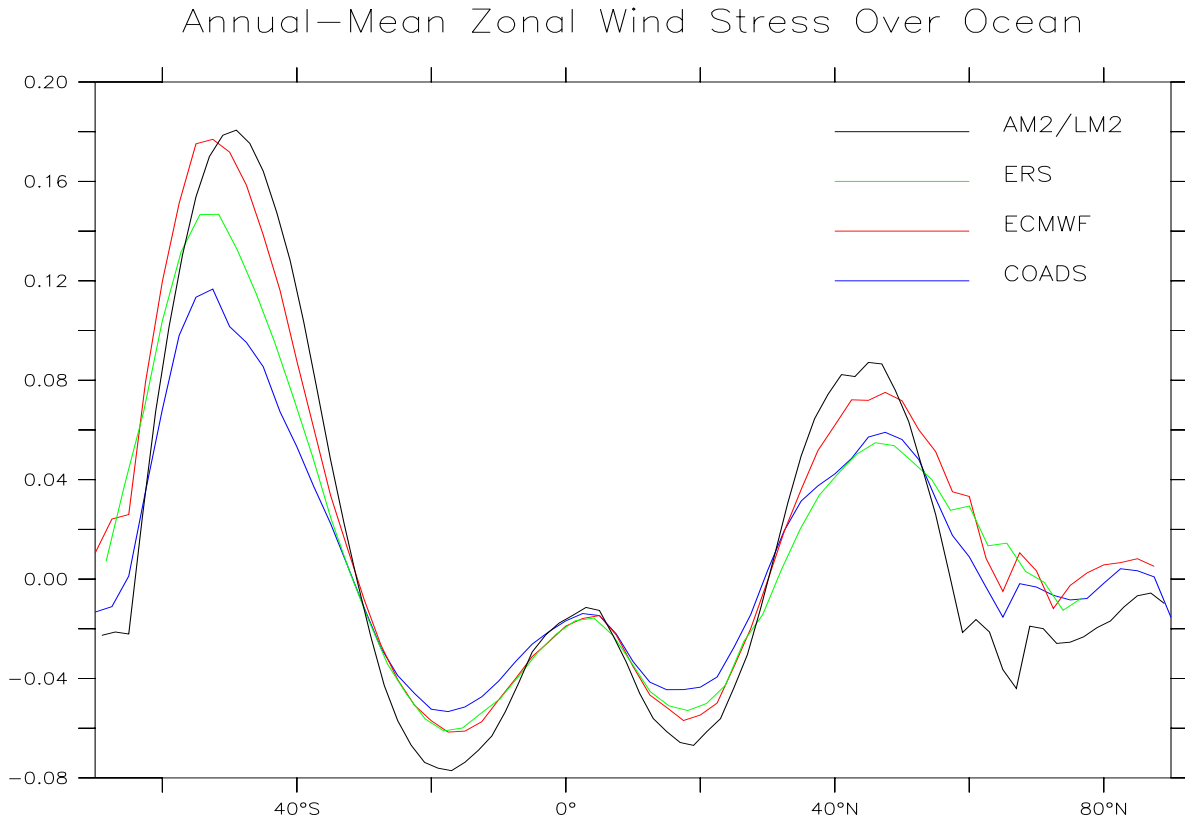
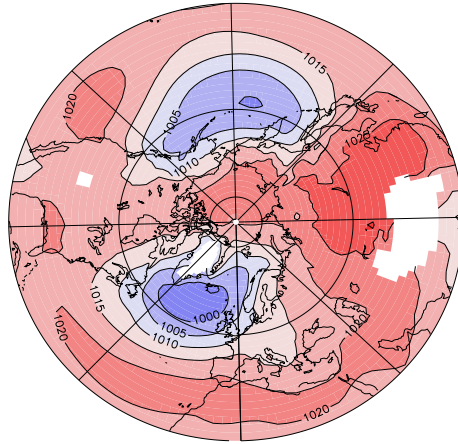
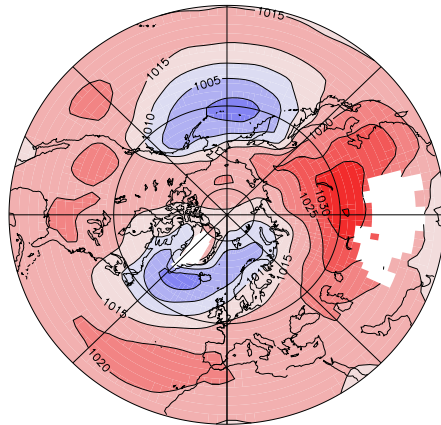


Figure 5. Long-term annual and zonal mean zonal wind stress in Pa over the ocean for the ship-based climatology of COADS (blue) (daSilva et al. 1994; Woodruff et al. 1987), ECMWF reanalysis (red), the ERS satellite scatterometer (green) (CERSAT-IFREMER 2002), and AM2/LM2 (black). The sign convention is such that a positive stress indicates an easterly stress on the atmosphere and a westerly stress on the ocean.

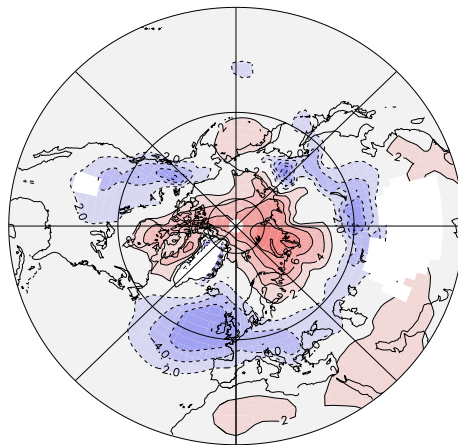
GFDL GAMDT



AM2/LM2



Reanalysis

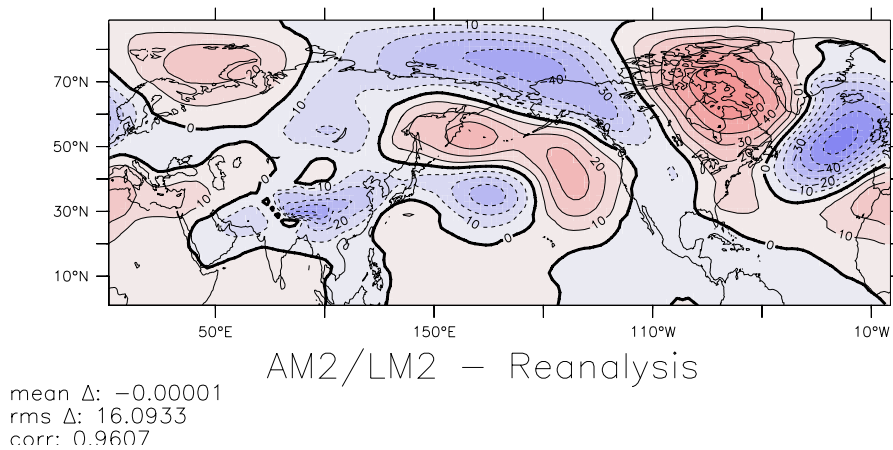
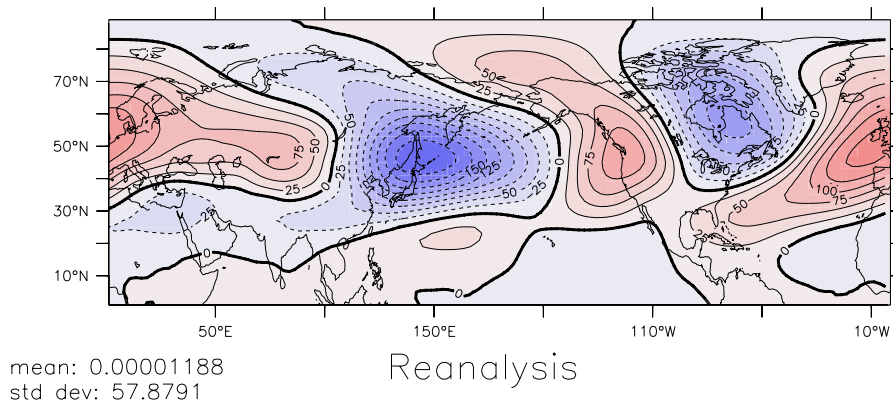
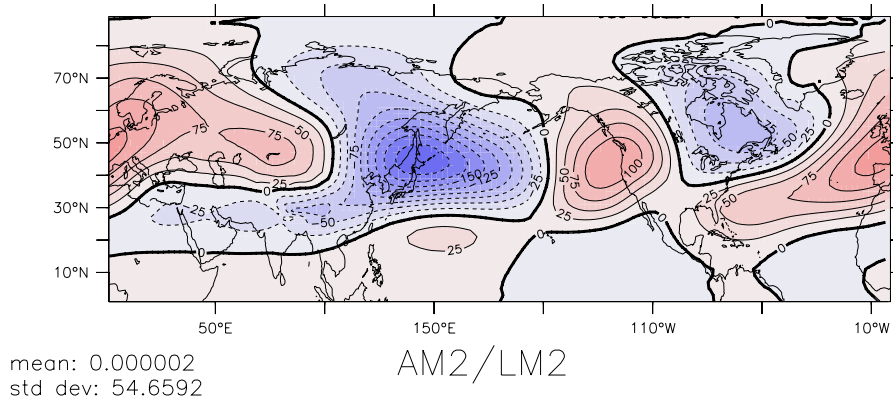


AM2/LM2 - Reanalysis

Figure 6. Long-term Northern Hemisphere DJF mean SLP for (a) AM2/LM2, (b) NCEP/NCAR reanalysis, and (c) AM2/LM2 minus NCEP. Contour interval is 5 hPa for (a) and (b) and 2 hPa for (c); the zero contour is not plotted in (c). Note that regions with mean surface pressure below 750 hPa have been masked.

GFDL GAMDT

Z*500, djf



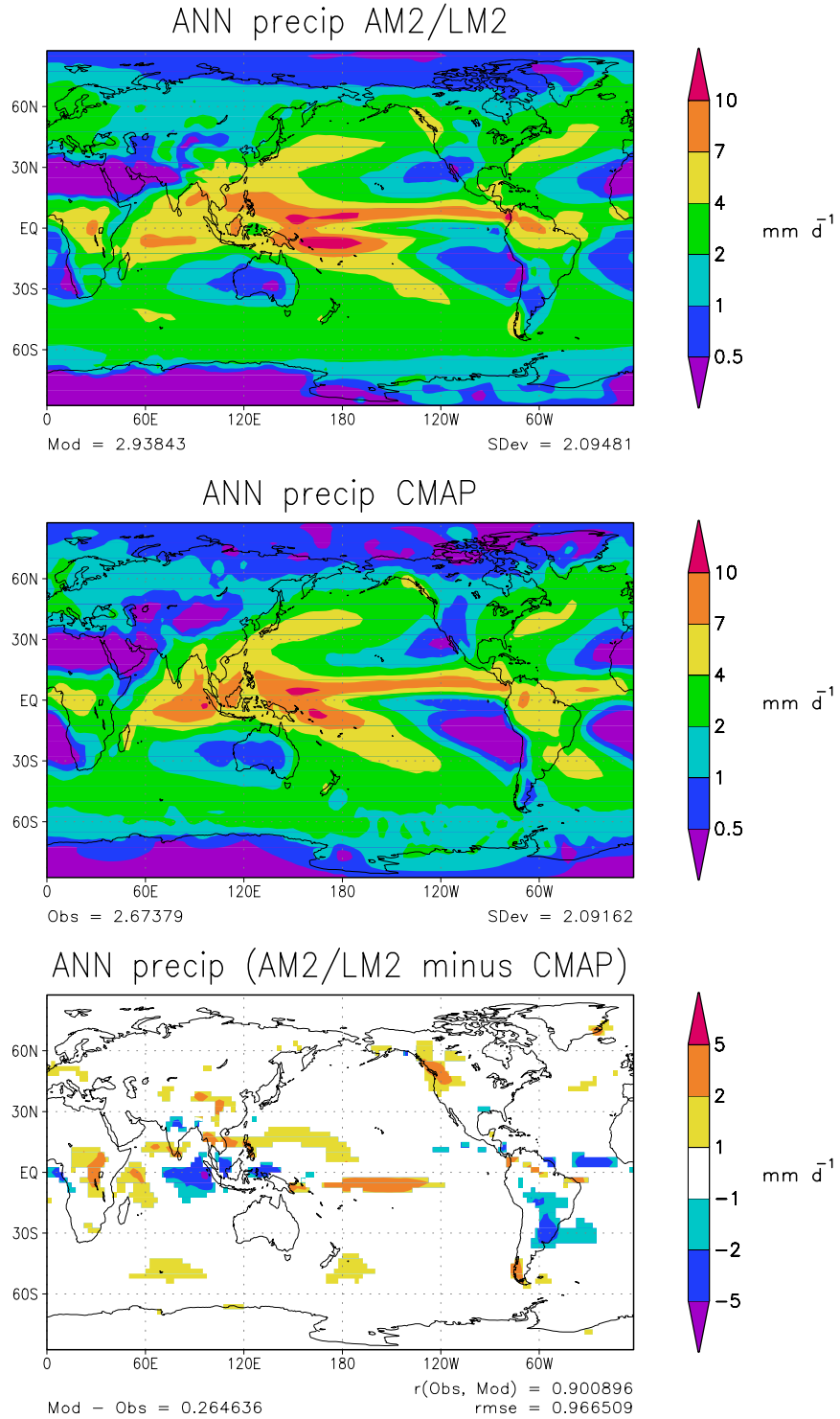


Figure 8. Annual long-term mean precipitation in mm d^{-1} for (a) AM2/LM2, (b) CMAP observations, and (c) AM2/LM2 minus CMAP. Statistics at the bottom of (a) and (b) include the global mean and standard deviation. Statistics at the bottom of (c) include the difference in global means, the correlation coefficient, and the root mean square error.

GFDL GAMDT

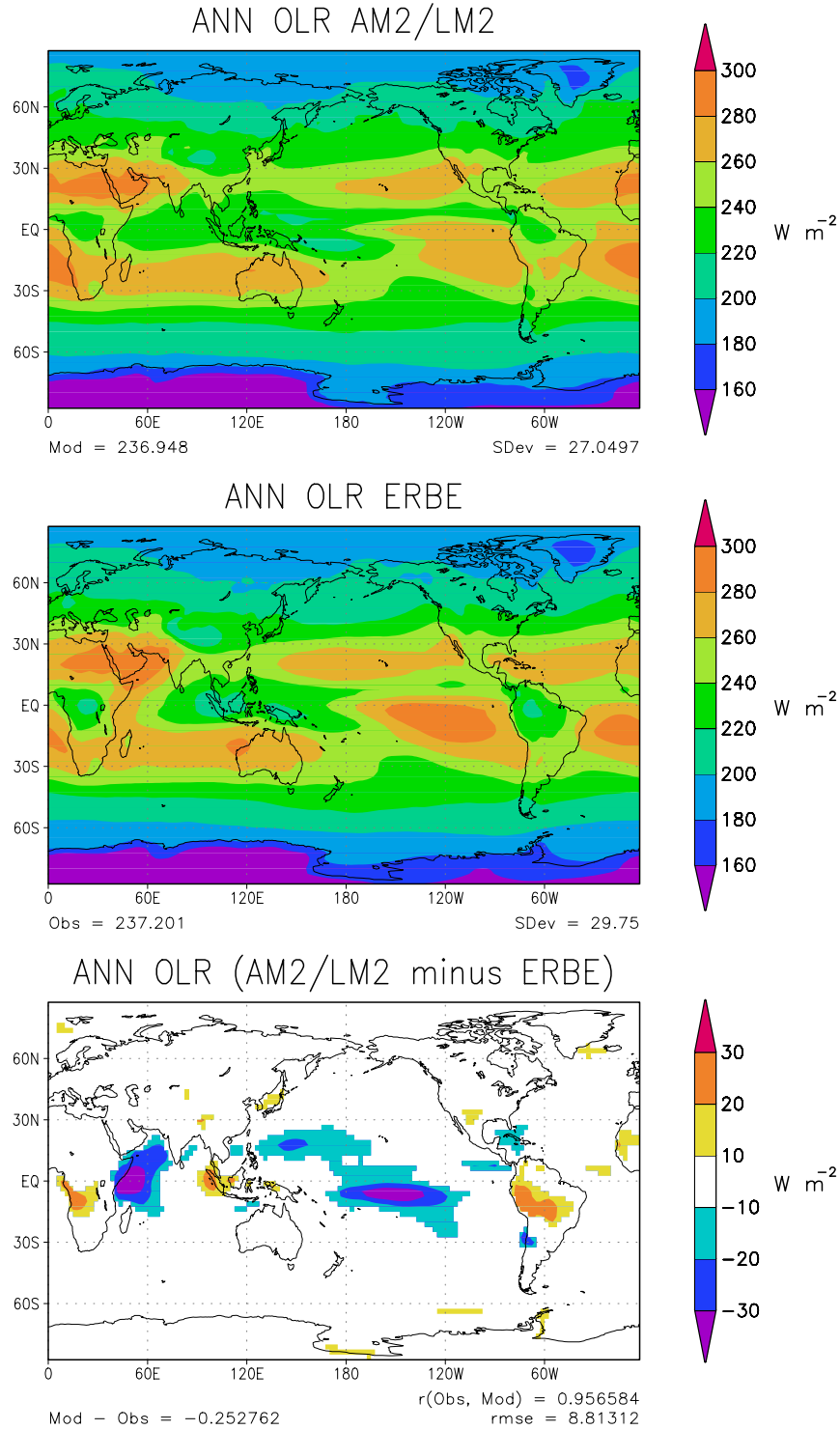


Figure 9. Annual long-term mean outgoing longwave radiation (OLR) in W m^{-2} for (a) AM2/LM2, (b) ERBE observations, and (c) AM2/LM2 minus ERBE. Statistics at the bottom of (a) and (b) include the global mean and standard deviation. Statistics at the bottom of (c) include the difference in global means, the correlation coefficient, and the root mean square error. Note that the original ERBE observations have been scaled so they have a global annual mean of 237.2 W m^{-2} .

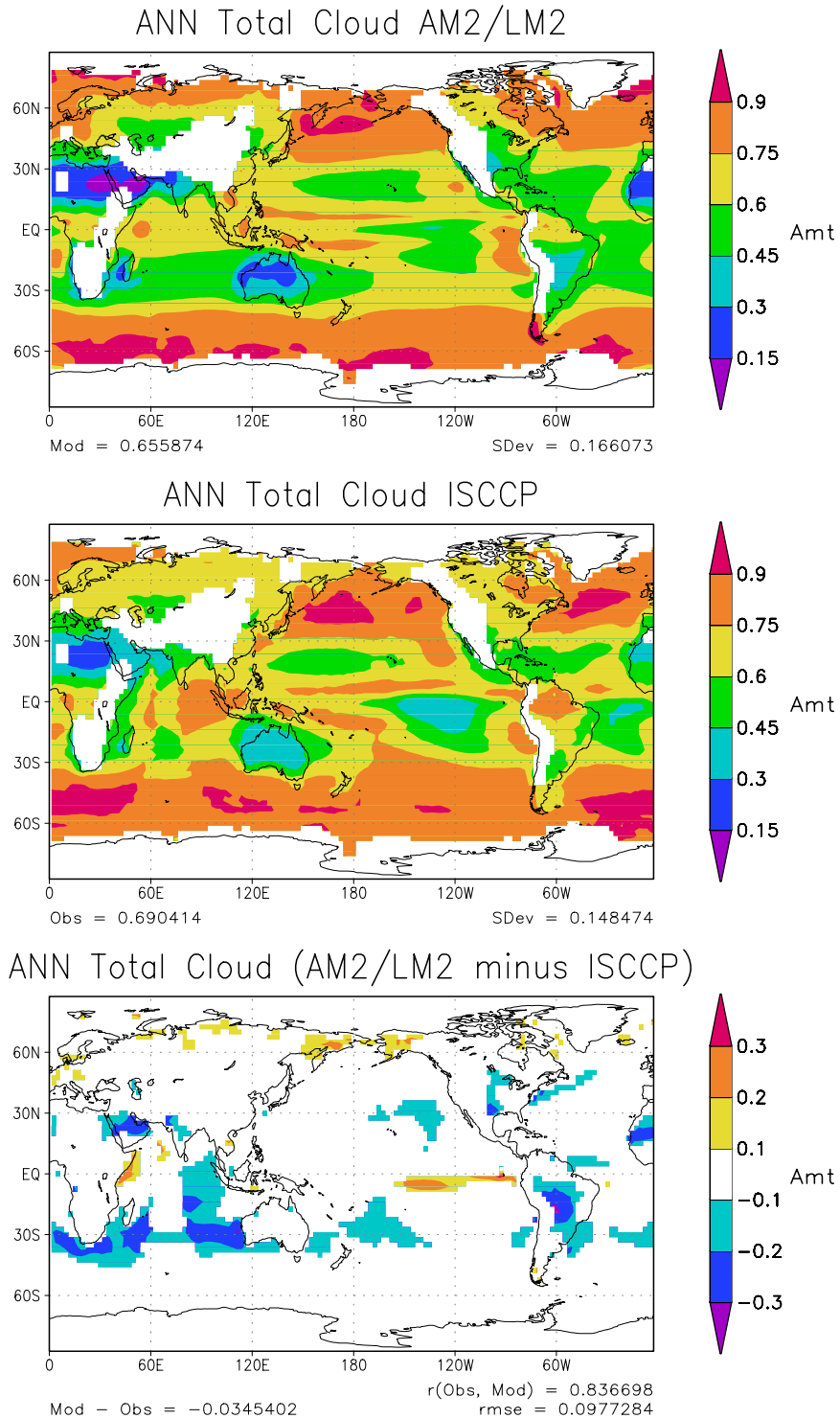


Figure 11. Annual long-term mean total cloud amount (fraction) for (a) AM2/LM2, (b) ISCCP observations, and (c) AM2/LM2 minus ISCCP. Statistics at the bottom of (a) and (b) include the global mean and standard deviation. Statistics at the bottom of (c) include the difference in global means, the correlation coefficient, and the root mean square error. Regions with snow or ice at the surface or a surface elevation greater than 1000 m are not shaded in (a) or (b) as the ISCCP satellite estimates at these points are deemed unreliable.

GFDL GAMDT

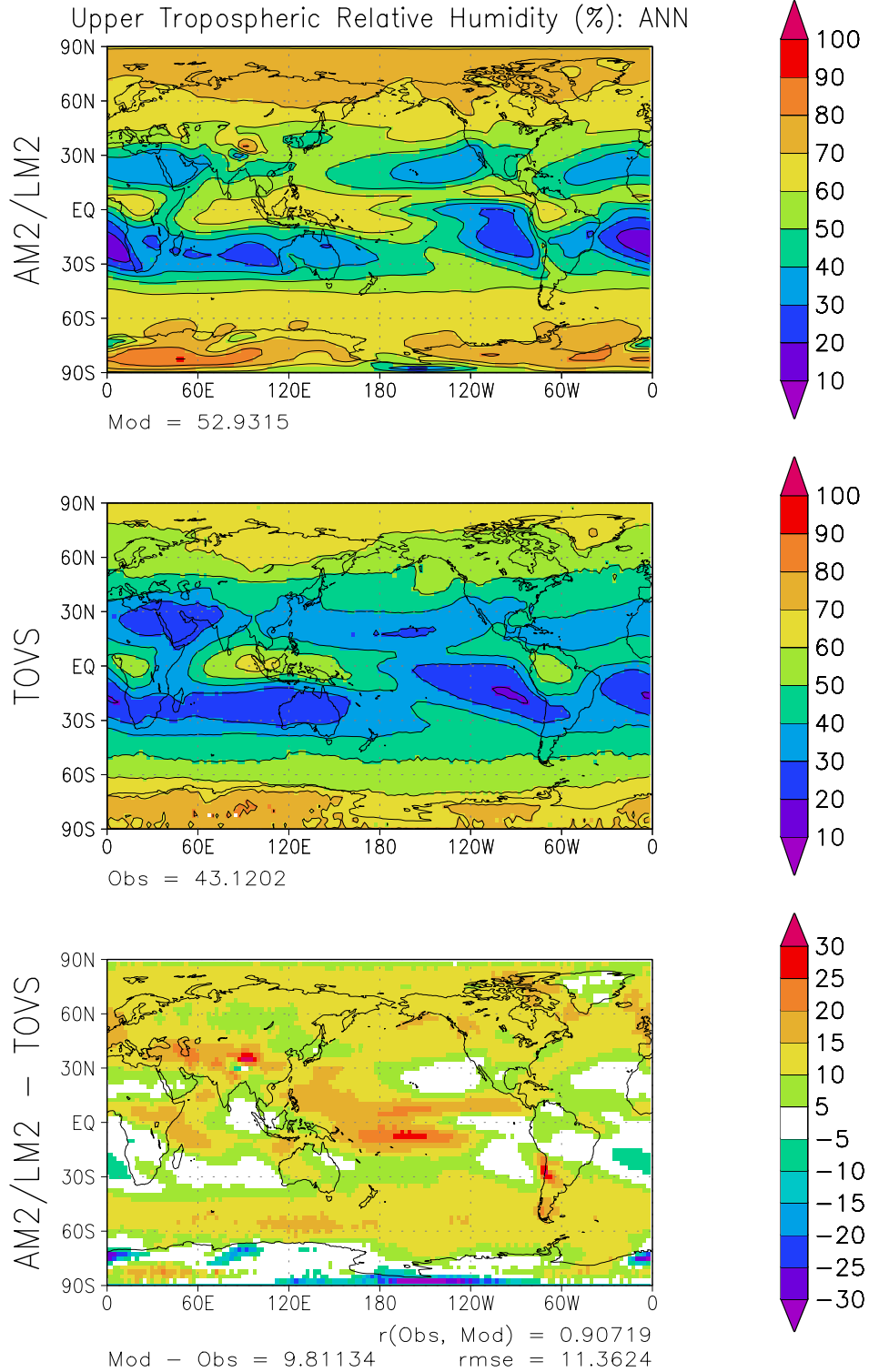
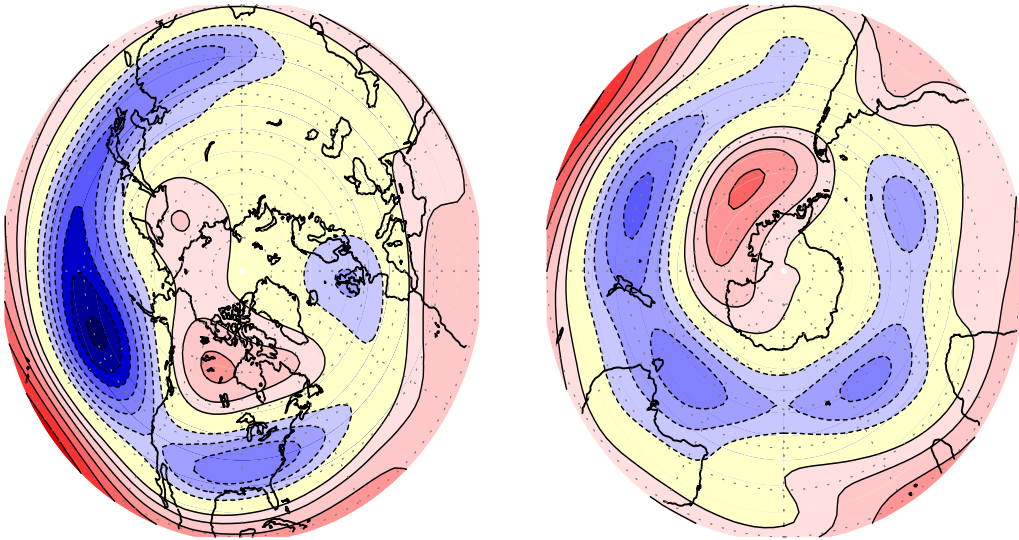


Figure 12. Annual long-term mean upper tropospheric humidity in percent for (a) AM2/LM2, (b) TOVS observations, and (c) TOVS minus AM2/LM2. Statistics at the bottom of (a) and (b) indicate the global mean. Statistics at the bottom of (c) include the difference in global means, the correlation coefficient, and the root mean square error.

Model



Observations

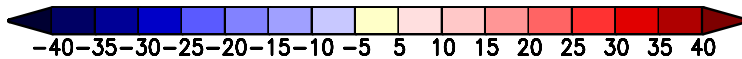
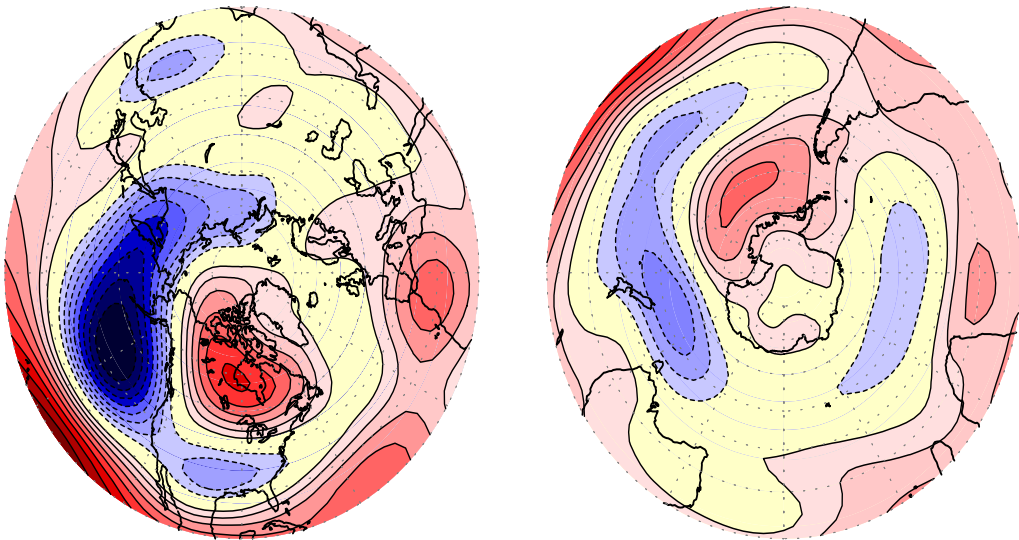


Figure 13. Distributions of the regression coefficients of 200 hPa height versus the standardized NINO3 SST index, as computed using the ensemble mean of the 10-member AMIP-style integrations with the AM2/LM2 (upper panels) and NCEP reanalyses (lower panels) for the December-January-February season of the 1951-2000 period. Results for the northern and southern extratropics are shown in the left and right panels, respectively. Contour interval is 5 m. The zero-contour is not plotted.

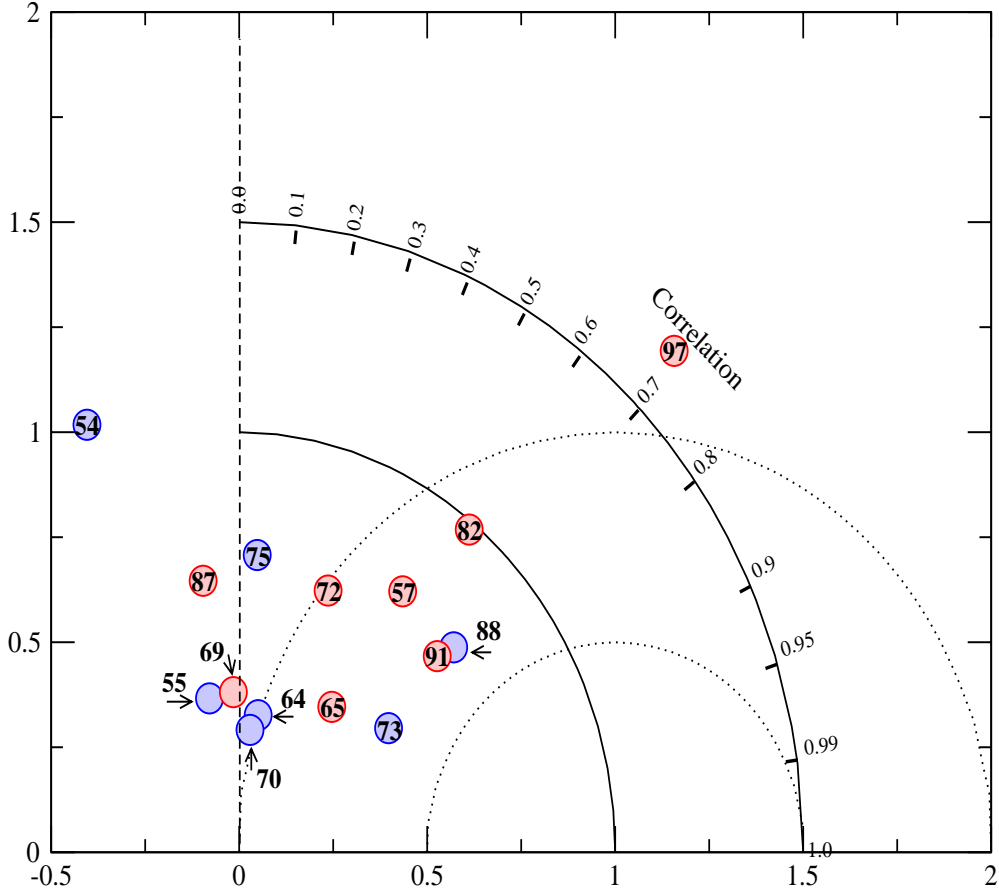


Figure 14. Taylor diagram depicting the relationships between the observed DJF 200 hPa height anomalies in the North Pacific / North American sector (20° - 70° N, 60° - 180° W) during selected ENSO events and the corresponding ensemble-mean patterns as simulated in the 10-member AMIP-style runs with the AM2/LM2. Results for individual warm and cold ENSO events are presented using red and blue dots, respectively. The two-digit label for each dot indicates the year of the event in question. The spatial correlation coefficient is given by the cosine of the angle between the abscissa and the straight line joining the origin and the dot representing the event of interest; correlation values are given along the outer solid arc. The ratio between the simulated and observed spatial variances is given by the distance between the dot and origin; inner and outer solid arcs indicate ratios of 1 and 1.5, respectively. The root mean square (rms) difference between the simulated and observed pattern, as normalized by the spatial variance of the observed field, is given by the distance between the dot and the point with coordinates (1,0) in the diagram; inner and outer dotted arcs indicate normalized rms differences of 0.5 and 1, respectively.

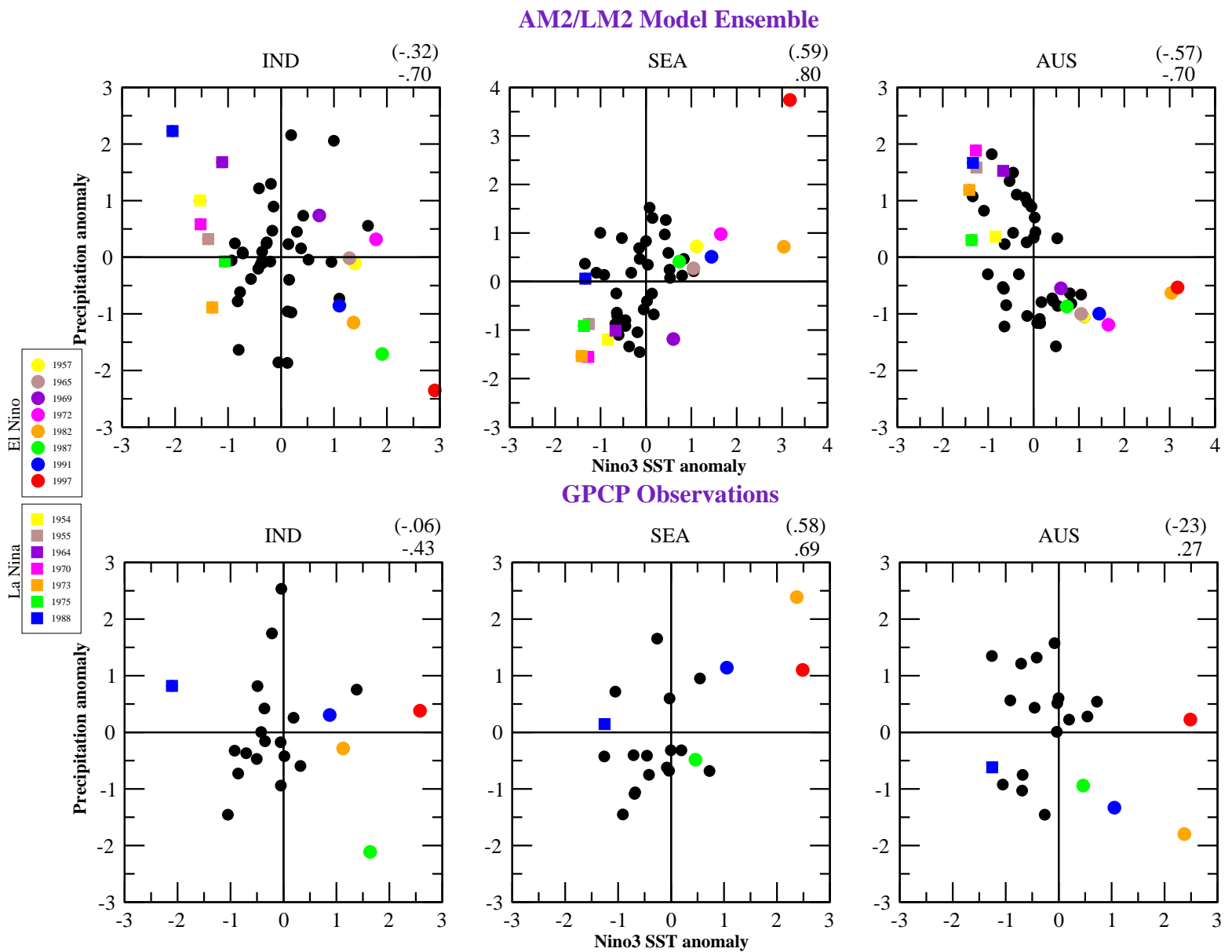


Figure 15. Scatterplots of the precipitation anomalies in three monsoon regions [IND - Indian; AUS - northern Australia; SEA - southeast Asia; boundaries of these regions are depicted in Figure 3 of Lau and Nath (2000)] versus the NINO3 SST anomalies. The abscissa in all panels represents the standardized SST anomaly in the NINO3 region. The ordinate axis represents the standardized precipitation anomaly in IND during the JJA season (left panels), and in SEA (middle panels) and AUS (right panels) during the DJF season. The upper panels are based on AM2/LM2 output for the 1951-2000 period. The lower panels show the observational estimates provided by GPCP for the shorter period of 1979-2000. In each panel, the anomalies of precipitation and NINO3 index for a given year are jointly depicted by a small dot or square. The outstanding warm and cold ENSO events are highlighted using colored dots and squares, respectively. The data for all remaining years are plotted using black dots. The correlation coefficient for the data entries in each panel is shown in the upper right corner of that panel. Correlation values based on all available years are given in parentheses. Correlation values based on the available warm and cold ENSO events only are given without parentheses.

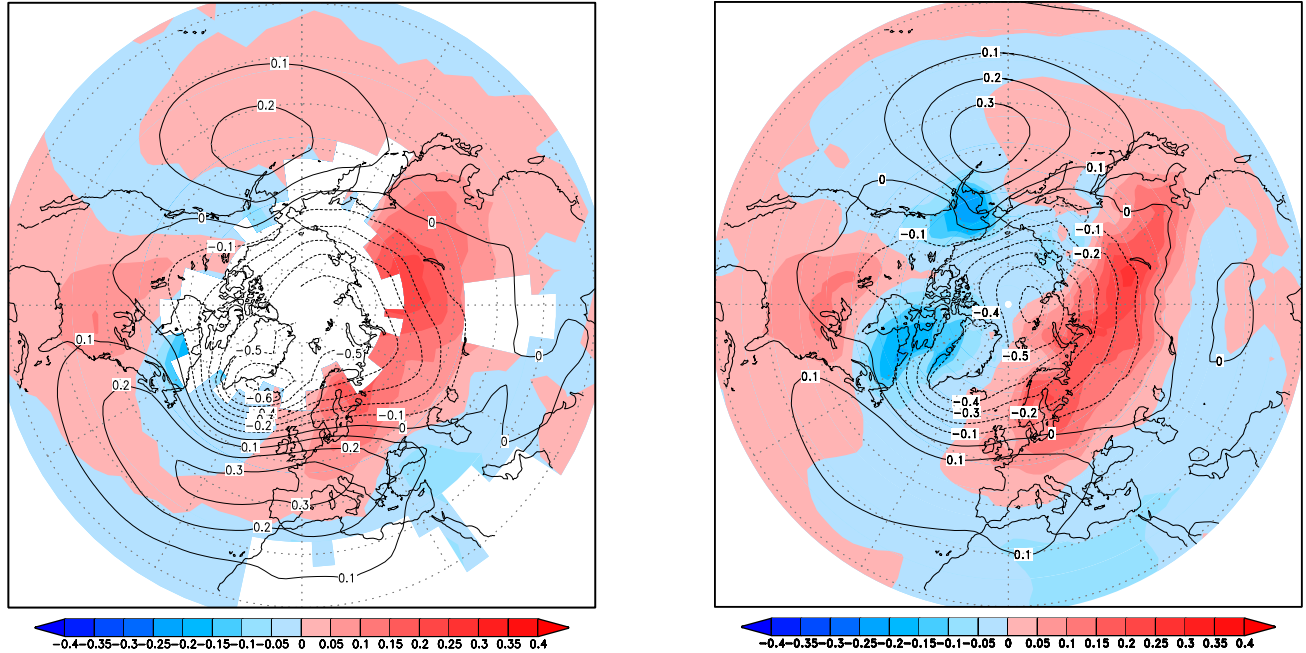


Figure 16. Spatial pattern of the Northern Annular Mode (NAM) and associated temperature anomalies for the months of November through April. The NAM is defined by computing an empirical orthogonal function (EOF) of SLP for all points north of 20°N. An NAM index is then calculated as the difference between the minimum and maximum of the spatial pattern of the first EOF multiplied by its associated time series, thereby yielding an index with units of hPa. The contours indicate the linear regression coefficients of SLP at each grid point versus an index of the NAM. The color shading indicates the linear regression coefficients on the NAM index of surface temperature at each grid point. The left panel displays analyses from observational data of SLP (Thompson and Wallace 1998), land surface air temperature (Jones 1994), and SST (Jones 1994). The right panel displays AM2/LM2 model results based upon one of the 50 year ARCs integrations. The model calculation uses surface air temperature over both land and ocean.

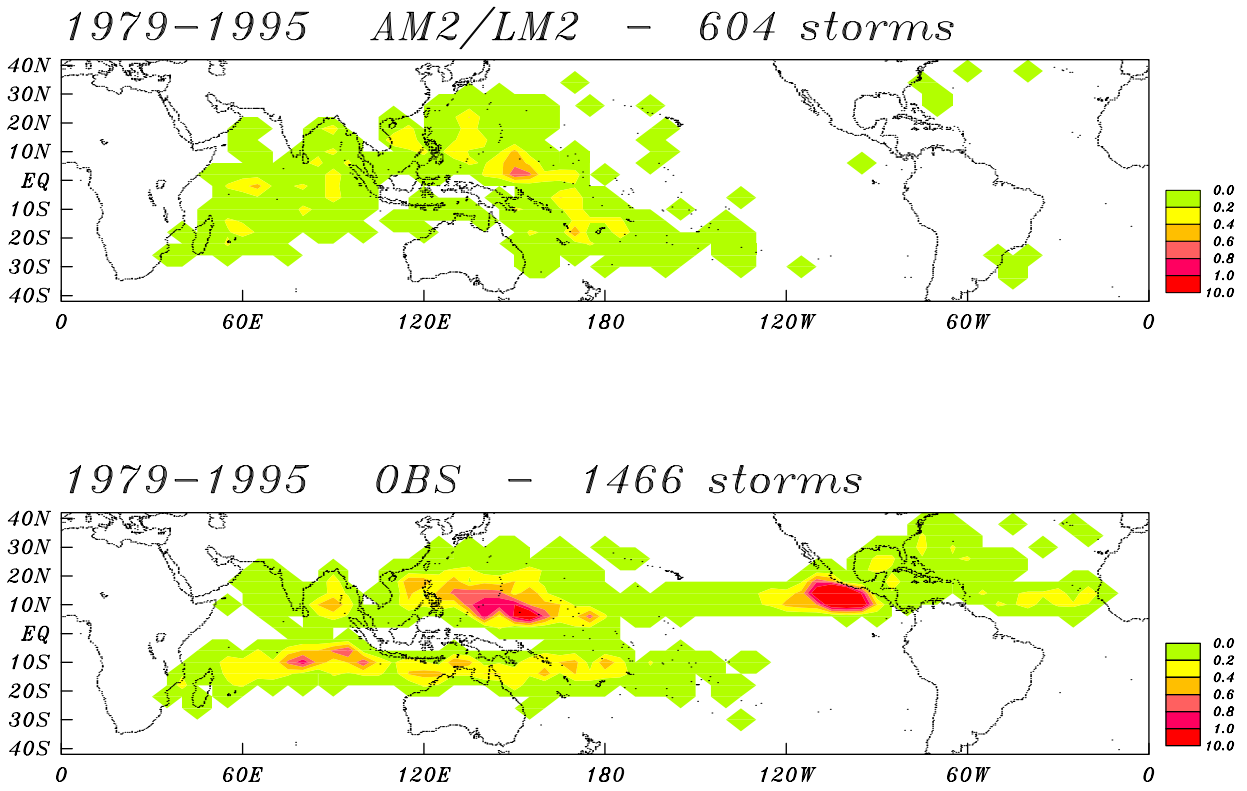


Figure 17. Frequency of tropical storm genesis for (a) observations and (b) AM2/LM2. Units are number of storms per year in a box of size 4° latitude by 5° longitude.

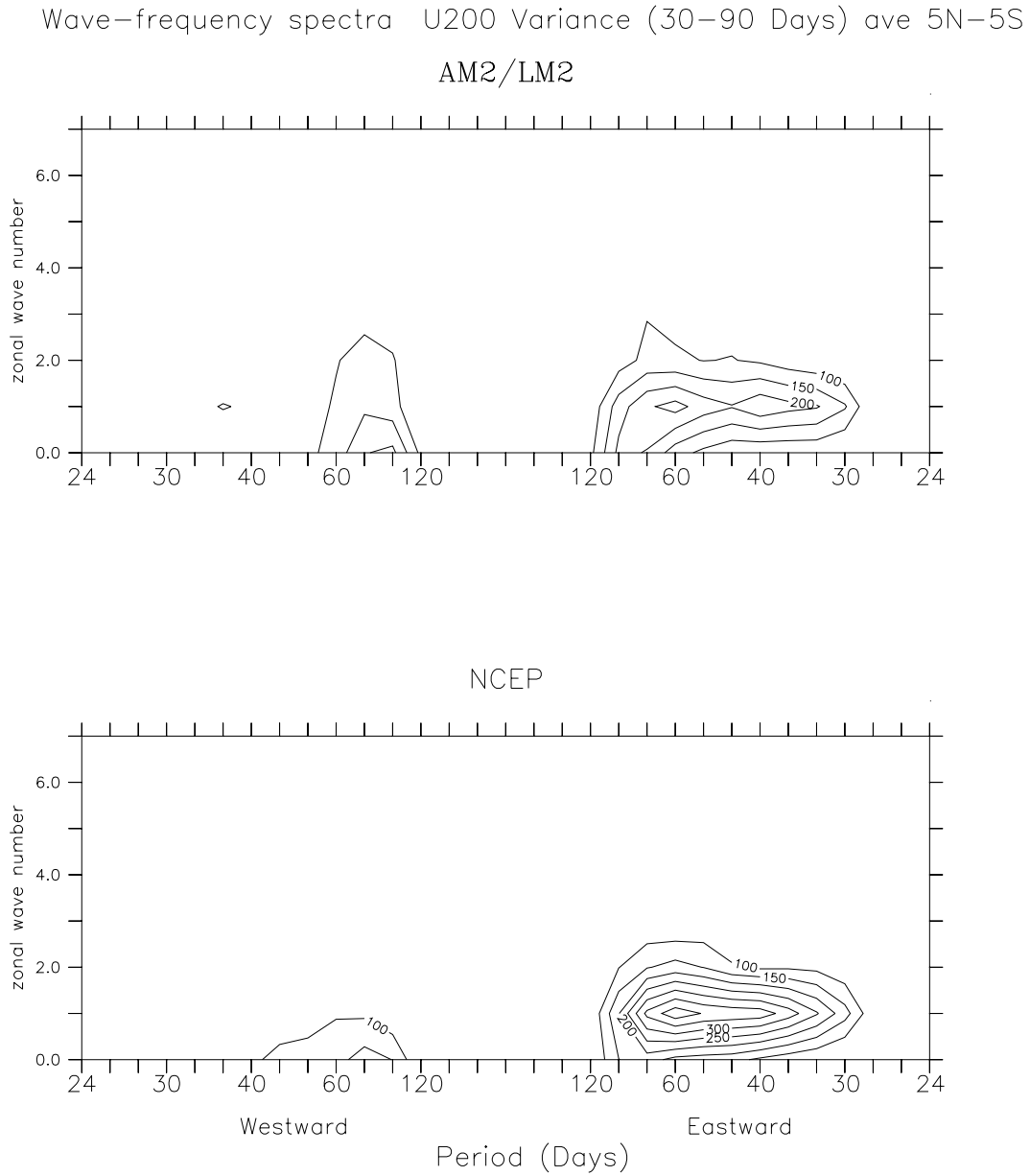
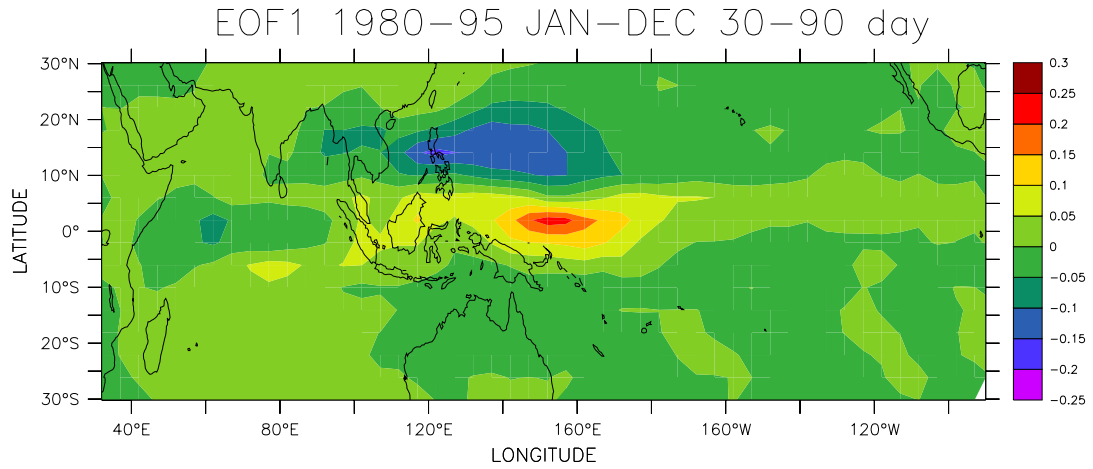
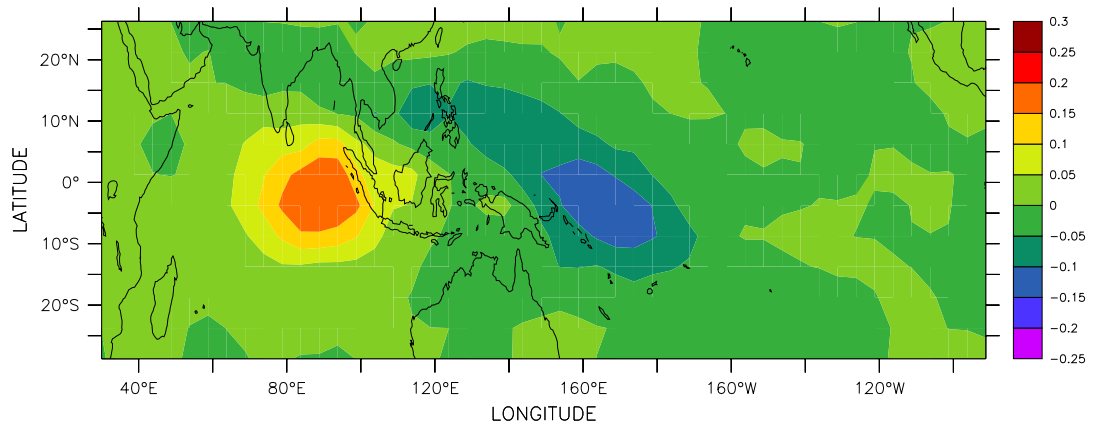


Figure 18. Wave frequency spectra of the variance of 30 to 90 day band-passed 200 hPa zonal wind, averaged for the period 1980 to 1995, for (a) AM2/LM2 and (b) NCEP reanalyses. Contour interval is $50 \text{ m}^2\text{s}^{-2}$.



AM2/LM2

Frac Variance = 0.042166



CMAP

Frac Variance = 0.1047

Figure 19. First EOF of 30 to 90 day band-passed precipitation, for the period 1980 to 1995, for (a) AM2/LM2 and (b) CMAP. Units are mm d^{-1} .

GFDL GAMDT

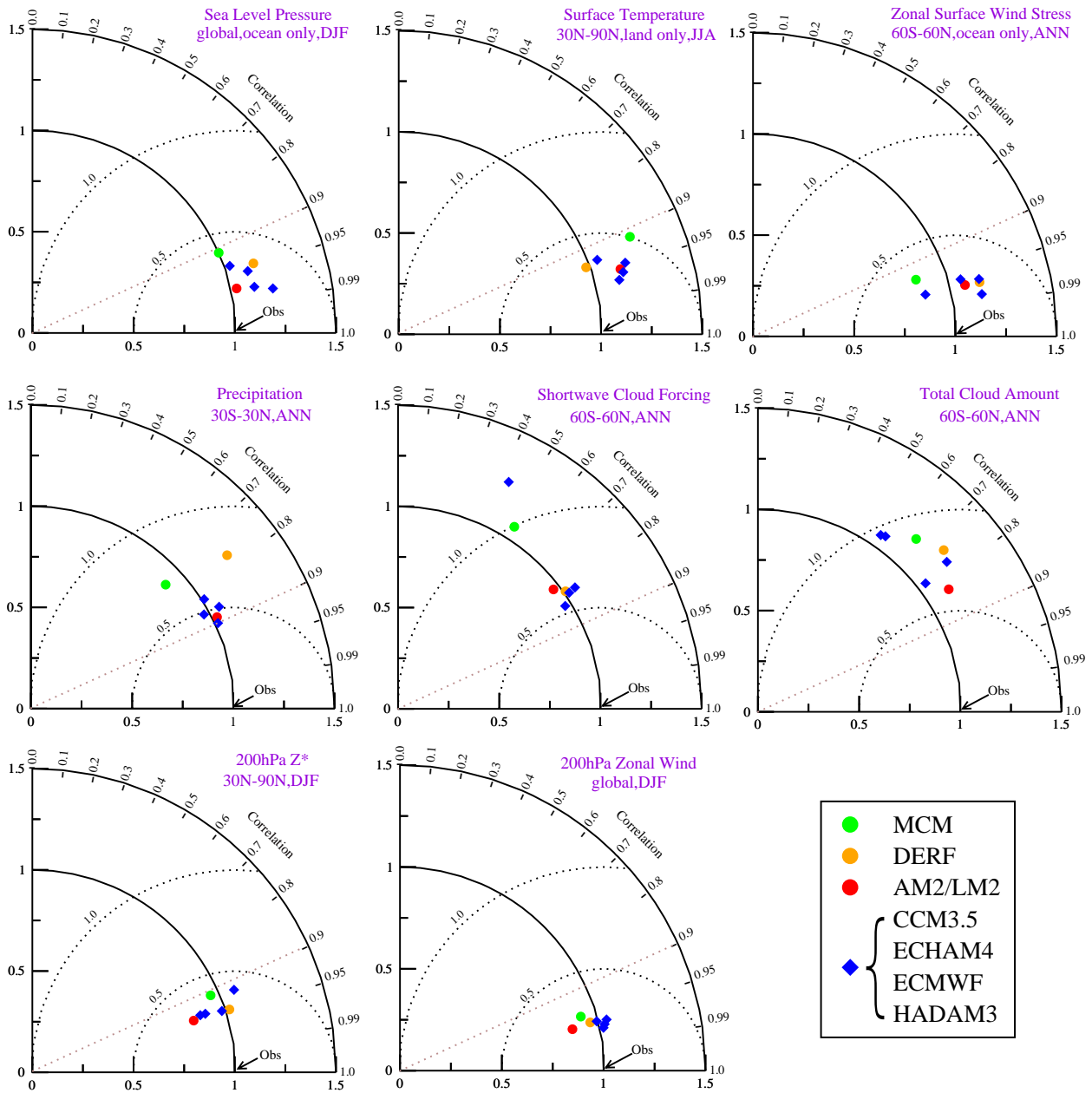


Figure 20. Taylor diagrams for selected variables comparing the skill of AM2/LM2 (red circle) in reproducing the observed climatology to that of older GFDL models (MCM and DERF, green and orange circles respectively) and other models participating in AMIP II (CCM3.5, ECHAM4, ECMWF, and HADAM3). Note that all non-GFDL models are plotted with a blue diamond to prevent unique identification. The selected variables include those associated with surface climate (SLP, land surface air temperature, and oceanic wind stress, top row), hydrology and clouds (precipitation, shortwave cloud forcing, and total cloud amount, middle row), and upper tropospheric circulation (200 hPa eddy geopotential and zonal wind, bottom row). The observational sources for these data include the NCEP reanalyses for SLP and 200 hPa eddy geopotential and zonal wind, ECMWF reanalyses for oceanic wind stress, ERBE for cloud radiative forcing, ISCCP for total cloud amount, CMAP for precipitation and CRU for land surface air temperature. Beneath each variable name is an indication of the geographical domain and season used in the calculation.

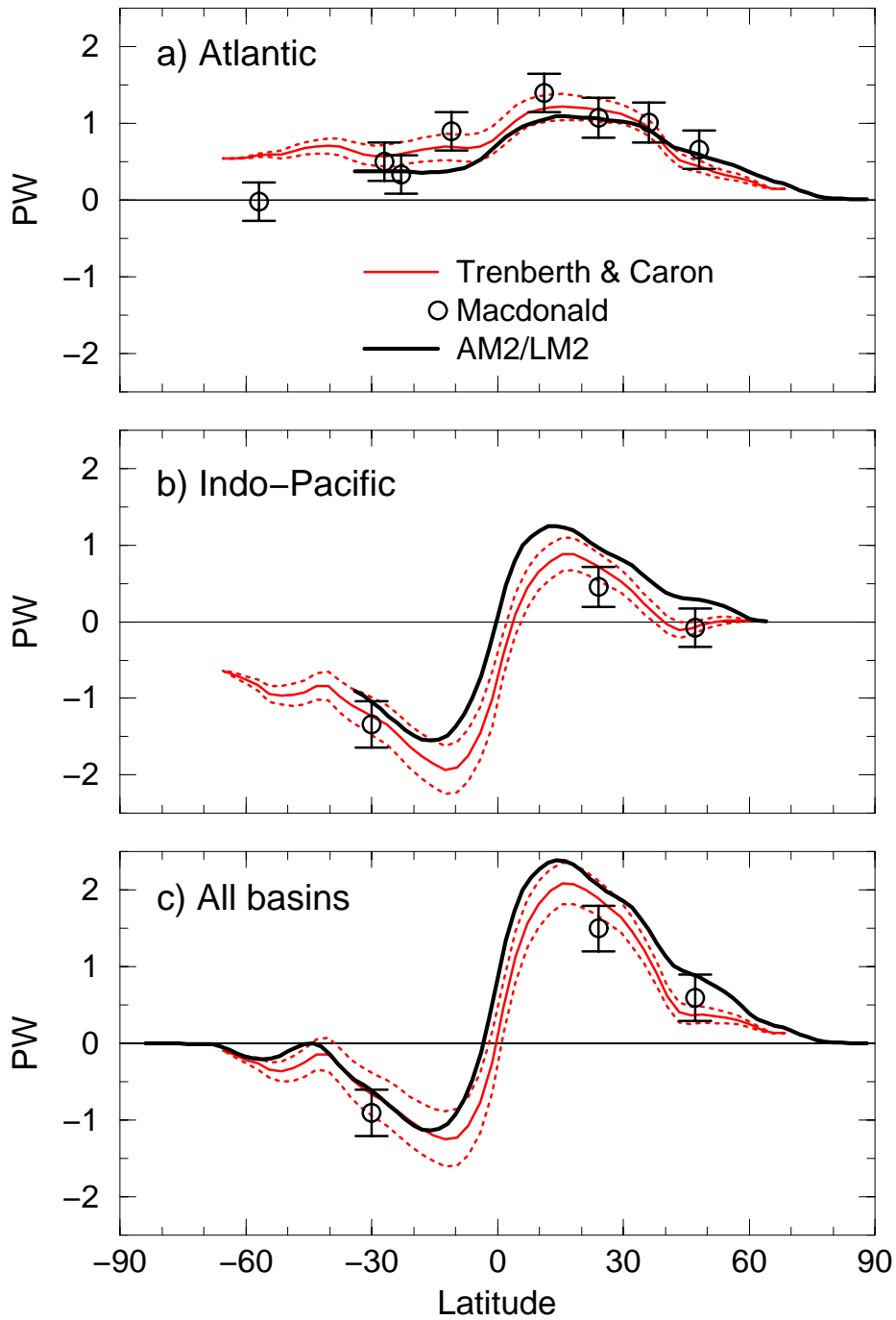


Figure 21. Poleward oceanic heat transport in petawatts (10^{15} W) from observational based estimates and implied by AM2/LM2 (dark black line). The observed estimates are derived from atmospheric data (Trenberth and Caron 2001; red lines with dashed lines indicating plus or minus one standard error; based on NCEP-derived products) or oceanic data (MacDonald 1998; their Table 20; circles with error bars). Results are shown for the a) Atlantic, b) Indo-Pacific, and c) world ocean basins.